Exact Solutions and Upscaling for 1D Two-Phase Flow in Heterogeneous Porous Media

Kofi Ohemeng Kyei Prempeh, Parker William George, and Pavel Bedrikovetsky

School of Chemical Engineering, The University of Adelaide, 5005 Adelaide, SA, Australia

Corresponding author: Pavel Bedrikovetsky (pavel.bedrikovetski@adelaide.edu.au)

Key Points:

- Exact solutions for 1D two phase flows in heterogeneous porous media
- Implicit formula for upscaling x-dependent fractional flow function
- Flux-history and saturation-profile based upscaling yield the same equation for fractional flow

Abstract

Upscaling of 1D two-phase flows in heterogeneous porous media is important in interpretation of laboratory coreflood data, streamline quasi 3D modelling, and numerical reservoir simulation. In 1D heterogeneous media with properties varying along the flow direction, phase permeabilities are coordinate-dependent. This yields the conservation law (Buckley-Leverett equation) with coordinate-dependent fractional flow $f=f(s,x)$, which reflects the heterogeneity. So, an x-dependency is considered to reflect microscale heterogeneity and averaging over x – upscaling. This work aims to average or upscale the heterogeneous system to obtain the homogenised media with such fractional flow function $F(S)$ that provides the same water-cut history at the reservoir outlet, x=1. Thus, $F(S)$ is an equivalent property of the medium. Despite the availability of numerous methods for upscaling of two-phase flow in porous media, the exact upscaling for 1D micro heterogeneous systems has not been derived. With the x-dependency of fractional flow, the Riemann invariant is flux f, which yields exact integration of 1D flow problems. The novel exact solutions are derived for flows with continuous saturation, transition of shock into continuous wave, transition of continuous wave into shock, and transport in heterogeneous piecewise-uniform rocks. The exact procedure of upscaling from $f=f(s,x)$ to $F(S)$ is as follows: the inverse function to the upscaled $F(S)$ is equal to the averaged saturation over x of the inverse microscale function $s=f^{-1}(f,x)$. It was found that the Welge's method as applied to heterogeneous cores provides the upscaled $F(S)$. With different arrangements of two homogeneous sections, analytical modelling shows completely different saturation distributions in the composite cores, while the upscaled saturation distributions are the same. For characteristic finite-difference scheme, the fluxes for microscale and upscaled-over-numerical-cells systems, coincide at all grid nodes.

Plain Language Summary

Natural or industrial two-phase flow of CO_2, water and other fluids occurs in highly heterogeneous porous media. The flow dynamics is modelled by transport equations with highly oscillating coefficients, which require extensive computational resources. This study aims to develop an upscaling technique for the domain-dependent flux resulting from the heterogeneity of the porous medium. The upscaling technique relies on the flux history (water-cut) and saturation profiles across the porous medium. It is determined that, for a given sequence or configuration of numerical cells or laboratory core samples, the upscaling of the domain dependent flux is achievable by saturation averaging. It is observed that results from water-cut based upscaling depend on length L while those of saturation profile-based upscaling depends on the time interval T.

1. Introduction

Two-phase flows in porous media occur in subterranean gas storage, including CO_2 and hydrogen, hydrology of unsaturated aquifers, vadose zone dynamics, plant irrigation, and commingled production of oil or natural gas with water (Ringrose, 2020). Figure 1a shows the schematic for the segregated flow of light gas above heavier water in a heterogeneous formation to depict the region of water saturation s and fractional flow of water f. Two-phase one-dimensional (1D) flows of immiscible incompressible fluids in homogeneous porous media and corresponding analytical solutions are presented in numerous books and papers; here we give only a brief incomplete sketch. Two-phase transport in rocks imposes extension of Darcy's law for each phase, introducing phase permeability for each phase, defined by Buckley and Leverett (1942); Rapoport and Leas (1953). Two-phase permeabilities versus saturation S, which is the volumetric concentration of water in water-gas fluid, are independent model functions defined by properties of the rock and two fluids. Mass balance of water for 1D flows yields the following hyperbolic equation

$$\frac{\partial S}{\partial t}+\frac{\partial F(S)}{\partial x}=0, \tag{1}$$

where S is the saturation (volumetric concentration) of water, and $F(S)$ is the water flux, called the fractional flow function (FFF). Some plots of FFFs are shown in Figure 1b.

1D two-phase flows with gravity for various phases (water, gas, oil) yield convex, concave, S-shaped and even non-monotonic fractional flow functions(Bedrikovetsky, 1993; Lake et al., 2014). Two dimensional (2D) flows in layer-cake reservoirs and reservoirs with stochastic heterogeneity can be averaged up to 1D flows in several asymptotic

cases including viscous, capillary, gravity domination and some combined regimes. The incomplete and brief reference list includes; Bruining (2021); Ingsøy et al. (1994); Kurbanov (1961): Yortsos (1995); Zhang et al. (2011). These cases yield even more complex forms of fractional flow functions.

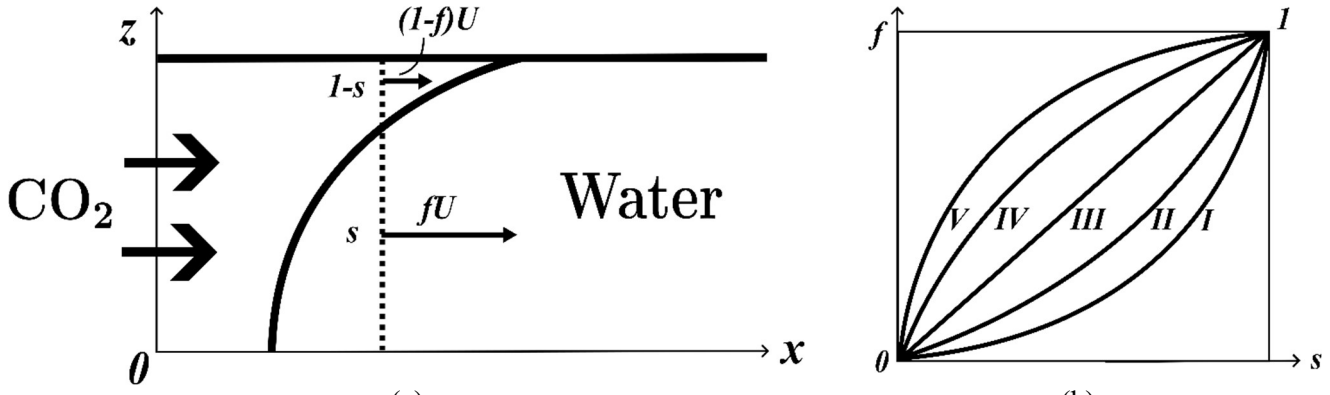

(a) (b)

Figure 1. Schematic for displacement of water by gas: a) segregated water-CO_2 flow; b) concave and convex fractional flow curves (FFCs).

Convex curves I and II in Figure 1b are encountered during gas-water flows in water-wet rocks, where water flux is low due to low gas viscosity and low relative permeability for water. This effect becomes even more pronounced for flow in layer-cake reservoirs dominated by gravity, where permeability decreases with depth. In such reservoirs, water flux is significantly reduced in the low-permeability layers closer to the reservoir bottom. For gas-oil flows, convex fractional flow curves (FFCs) result from the combination of low gas viscosities and acute oil-gas contact angles; meaning that the rock with connate water saturation is more oil-wet than gas-wet *Concave* FFCs IV and V in Figure 1b are typical for viscous-dominant cases in layer-cake reservoirs with water viscosity lower than the oil viscosity.

The injection of one phase into another phase yields the Riemann problem for 1D hyperbolic "Buckley-Leverett" equation. The solution to the 1D hyperbolic equation is self-similar; it depends on the variable group x/t (Barenblatt et al., 1990; Lake et al., 2014). The solutions for various forms of fractional flow consists of shock and rarefaction waves and can be found in basic books on conservation law systems (Dafermos, 1983; Logan, 2008; Polyanin & Manzhirov, 2006; Polyanin & Zaitsev, 2003; Zhang et al., 2011), as well as, monographs on flow in porous media (Barenblatt et al., 1990; Bedrikovetsky, 1993; Lake et al., 2014). In this paper, we discuss either concave or convex shape of $F(S)$ curves (Figure 1b).

Fractional flow curve $F(S)$ can be determined from the water-cut measurements at the outlet $x=1$ during two-phase displacement by the method of Welge (1952). The total two-phase mobility can be determined from the measurements of pressure drop across the core (Johnson et al., 1959; Jones & Roszelle, 1978). These two methods can be extended to two-phase compositional displacements with known self-similar solutions (Borazjani et al., 2019). However, the distinguished feature of these inverse solutions is that it is defined by self-similarity of the direct problem only and is independent of the solution itself. This allows extending the inverse solutions for the cases where the direct self-similar solution is not known (Bedrikovetsky, 1993).

One-dimensional (1D) two-phase flows in heterogeneous porous media are frequently encountered in reservoir engineering of water resources and energy sector. The incomplete list of examples includes: (i) corefloods in piecewise-uniform composite cores; (ii) corefloods in long outcrop plugs with heterogeneity along the plugs (like in North Sea cross-bed-sets); (iii) in streamline reservoir simulation of quasi 3D flows with rock property variations along streamlines, where the streamlines cross layers with different properties or domains with different facies; (iv) upscaling in numerical cells, where the flow is transversal to layering, like during vertical flows (Datta-Gupta & King, 2007; Subramanian et al., 1999).

The heterogeneity here can be encountered at the scale significantly lower than the flow-unit scale, like in a single cell of a coarse numerical grid. In the above four examples, for single-phase flows, the heterogeneity is

mathematically expressed as coordinate-dependent absolute permeability. For two-phase flow, the heterogeneity is expressed as coordinate-dependency of phase permeability, given by Eqs. (B3, B4), yielding x-dependent fractional flow. Appendix A lists the assumptions for the model of two-phase flow in porous media. Equation for 1D two-phase transport of immiscible incompressible fluids in heterogeneous undeformable porous media follows from expressions (B8, B9) in Appendix B:

$$\frac{\partial s}{\partial t}+\frac{\partial f\left(s,x\right)}{\partial x}=0 \quad , \tag{2}$$

where s is the normalised water saturation and $f=f(s,x)$ is the coordinate-dependent fractional flow at the microscale.

Figure 2 shows the schematic of the numerical grid for finite-difference solution of Eq. (2). If the finer grid is not allowed by computational resources, but the fractional flow significantly varies with x, the averaging or upscaling procedure for FFF from $f(s,x)$ to $F(S)$ is required. However, the upscaling procedure of the FFF for two-phase 1D flows in heterogeneous porous media is not available. This results in cumbersome numerical small-scale calculations.

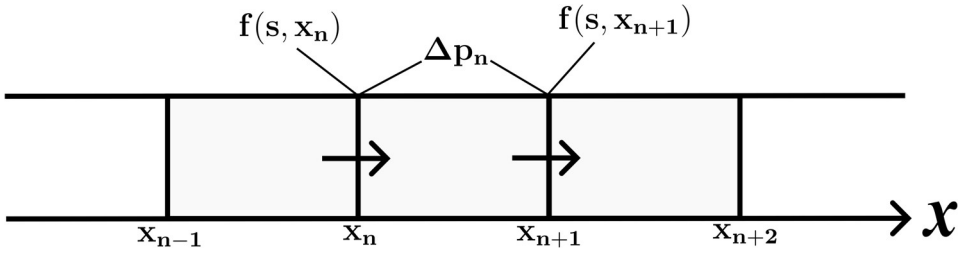

Figure 2. Numerical schema for solution of 1D two-phase transport equation.

Currently, upscaling of transport phenomena is under intensive development. Roberts (2022) developed a rigorous upscaling technique based on the theory of dynamic systems. More detailed derivations are presented by Roberts and Bunder (2017) for multidimensional spaces, and by Roberts (2015) and Tran-Duc et al. (2024) for quasi-periodic homogenisation, which was further generalised by Roberts (2024). A promising computational homogenisation is provided by the Equation-Free Patch Scheme such as that applied to beam dynamics in Roberts and Bunder (2017).

The detailed reviews on flow in porous media can be found from monographs by Das and Hassanizadeh (2005); Gray and Miller (2014); Bruining (2021); and Chung et al. (2023). For stochastic porous media, Shapiro and Bedrikovetsky (2008); Shapiro et al. (2007); Shapiro and Yuan (2012); Shapiro (2022, 2024), developed a random walk model, Boltzmann's equation, percolation model, and continuous upscaling, respectively. With the advent of machine learning, Elmorsy et al. (2023) presents permeability upscaling of three-dimensional (3D) rock based on physic-informed neural networks (PINN) models that learn from the analytical solution based on Darcy's law. Jiang et al. (2023) also presents a workflow to predict the upscaled absolute permeability of the rock core directly from CT images. The workflow employs deep learning techniques (neural networks) on raw CT images of rocks to generate upscaled permeability maps.

Another efficient and accurate upscaling scheme is provided by multi-resolution wavelet transformations (Moslehi et al., 2016; Rasaei & Sahimi, 2009; Rezapour et al., 2019). Rezapour et al. (2019) developed the wavelet transformations for cases in which the computational grid is totally unstructured.

Various numerical techniques based on local, global, or local-global upscaling have been developed by Barker and Dupouy (1999); Barker and Thibeau (1997); Chen and Durlofsky (2006); Chen and Li (2009); Darman et al. (2002). Upscaling can be performed by large-scale solution of inverse micro scale problems, or by optimal fitting of macro parameters (Cheng & Rabinovich, 2021; Moreno & Rabinovich, 2021; Wei & Rabinovich, 2023).

The work of Efendiev and Durlofsky (2004) adopts volume averaging and homogenisation techniques to generate modified coarse-scale convective flux function and coarse-scale diffusivity equation to characterize the interaction between local fine-scale effects and the global flow field, for each grid block. Li and Durlofsky (2016) present an upscaling procedure for oil or gas compositional flow simulation, where the upscaled parameters and functions

associated with each coarse-scale interface are computed from a global fine-scale simulations. The simulation accounts for transmissibility and relative permeability upscaling of flow properties, with further computation of component fluxes (Li & Durlofsky, 2016). Multiscale numerical hybrid grids can be used where the upscaled models do not exist in all parameter manifolds (Efendiev et al., 2016; Efendiev & Durlofsky, 2004). Exact upscaling is possible where an analytical solution at micro scale is available (Anto-Darkwah et al., 2021; Bedrikovetsky et al., 2019; Rabinovich et al., 2015; Rabinovich et al., 2016). However, exact upscaling for 1D two-phase flow in heterogeneous porous media, expressed by Eq. (2) is unavailable.

Radial two-phase flows with rate-dependent relative permeability can be described by Eq. (2) by using the expression of rate versus radius for incompressible flows (Mijic & LaForce, 2012; Mijic et al., 2014; Rossen et al., 2008; Rossen et al., 2011). These works adopt the constancy of the flux f along characteristics to construct semi-analytical approximate solutions of Eq. (2), while the current paper aims to derive exact solutions.

Despite the numerous approaches presented in literature, there remains the fundamental challenge of simplicity, accuracy, and fast determination of upscaled rock properties, including FFF. Present numerical upscaling techniques require extremely high computational power.

The current paper addresses the gap. For the first time, we derive exact solutions for flow with x-dependent fractional-flow for Riemann problems, and also for initial-boundary value problems with distributed data. The model limitation is negligible capillary pressure. The upscaled fractional flow function $F(S)$ for the distributed system $f(s,x)$ is defined by either the equality of flux histories at the outlet, or by the equality of profiles at a fixed moment. We derived a novel averaging procedure for saturation $s=f^{-1}(f,x)$ that results in implicit expression for $F(S)$. It was found that both definitions are equivalent and yield the same upscaling procedure. We proved that the upscaling in each numerical cell of characteristic finite-difference schema results in coincidence of fluxes at the nodes for distributed and upscaled systems.

The paper is structured as follows. Section 2 formulates the upscaling problem for first-order conservation law with x-dependent flux. Section 3 highlights the properties of an exact solution for initial-boundary value problems. Section 4 develops exact solutions for several Riemann problems. Section 5 derives exact solutions for non-Riemann problems. Section 6 defines the upscaling for 1D conservation law and derives formula for upscaled flux function $F(S)$. Section 7 applies the upscaling for 1D characteristic finite-difference model. Section 8 discusses the method limitations and possible extensions. Section 9 concludes the work.

2. Formulation of the problem

An initial-boundary value problem for Eq (2) is formulated as follows:

$$t=0:\ s=s_0(x), \tag{3}$$

$$x=0:\ f=f_0(t), \tag{4}$$

where $s_0(x)$ is the initial distribution of normalised saturation, and $f_0(t)$ is the inlet fractional flow of the injected water-gas fluid.

Below we will be using either of two formulations of boundary conditions (BCs): the inlet flux given by Eq. (4), or the corresponding saturation.

The initial and boundary conditions for Eq. (2), describing displacement of water by gas, yield the Riemann problem:

$$t=0:\ s=1, \tag{5}$$

$$x=0:\ f=0,\ s=0. \tag{6}$$

Eq. (2) for unknown $s(x,t)$ contains a model function – fractional flow function $f(s,x)$. The x-dependency of $f(s,x)$ is realised at lower scale for x-variation $0<x<1$. So, at the upper scale, the flux is independent of coordinate x; Eq. (1) determines unknown function $S(x,t)$.

We define upscaling as determining such function $F(S)$ that the outlet water flux $f_1(t)$ (produced volume of water) at $x=1$ is equal to that of the microscale system:

$$f\left(s\left(1,t\right),1\right)=F\left(S\left(1,t\right)\right)=f_1\left(t\right),\ 0<t<\infty. \tag{7}$$

Here macroscale saturation $S(x,t)$ and microscale saturation $s(x,t)$ are solutions of Eqs. (1) and (2), respectively.

Another definition of upscaling is the coincidence of saturation profiles for Eqs. (1) and (2) for any x at a fixed moment T:

$$s\left(x,T\right)=S\left(x,T\right),\ 0<x<\infty. \tag{8}$$

Section 5 shows the equivalence of both upscaling definitions.

3. Solutions for 1D flow problem

Let us derive the exact solution of initial-boundary problem (3, 4) for Eq. (2). Multiplying both sides of Eq. (2) by partial derivative of FFF with respect to s, $f'_s(s,x)$, yields

$$f'_s\frac{\partial s}{\partial t}+f'_s\frac{\partial f\left(s,x\right)}{\partial x}=0,\ \ f'_s\left(s,x\right)=\frac{\partial f\left(s,x\right)}{\partial s}, \tag{9}$$

where the first term can be expressed as time partial derivative of f. This transforms Eq. (9) to the form

$$\frac{\partial f\left(s,x\right)}{\partial t}+f'_s\frac{\partial f\left(s,x\right)}{\partial x}=0\ , \tag{10}$$

resulting in the following characteristic form of PDE (10):

$$\frac{dx}{dt}=f'_s,\ \frac{df}{dt}=0\ . \tag{11}$$

Eq (11) shows that fractional flow f is constant along the characteristics, i.e., f is Riemann invariant. This is the main feature of Eq. (2) used further to derive exact solutions (sections 4 and 5) and upscaling technique (sections 6 and 7). So, along the characteristics, saturation becomes a function of x:

$$f=f\left(s,x\right),\ s=f^{-1}\left(f,x\right). \tag{12}$$

Here f^{-1} is the inverse function to the fractional flow $f=f(s,x)$.

Substituting expression (12) into the equation for characteristic curve (11) yields

$$\frac{dx}{dt}=f'_s\left(f^{-1}\left(f,x\right),x\right). \tag{13}$$

Separating variables in the obtained ordinary differential equation (ODE) (13) yields the implicit solution for characteristic lines

$$t=\int_{x_0}^{x}\frac{dy}{f'_s\left(f^{-1}\left(f\left(s_0\left(x_0\right)\right),y\right),y\right)}\ . \tag{14}$$

Here the characteristic starts at point $(x_0,0)$ in (x,t)-plane, and constant f-value is determined from initial conditions (ICs) given by Eq. (3): $f=f(s_0(x_0), x_0)$. Implicit formula (14) for characteristic curve is obtained due to constancy of f along the characteristic.

For characteristics starting at point $(0,t_0)$, the trajectory is

$$t = t_0 + \int_0^x \frac{dy}{f_s'\left(f^{-1}\left(f_1(t_0)\right), y\right)} \quad . \tag{15}$$

For Riemann problem given by Eqs. (5, 6), $x_0=t_0=0$.

Either of trajectories by Eq. (14) or Eq. (15) expresses time versus x and f:

$$t = \tau(x, f). \tag{16}$$

Eqs. (14, 15) also allow calculating the time of arrival of the characteristics, carrying fractional flow $f=const$ to the outlet x=1:

$$t_f = \tau(1, f). \tag{17}$$

The Hugoniot-Rankine condition on a shock front $x_f(t)$ reflects mass balance that corresponds to conservation law (2), (Polyanin et al., 2001):

$$\frac{dx_f(t)}{dt} = \frac{f^+(t) - f^-(t)}{f^{-1}\left(f^+, x_f(t)\right) - f^{-1}\left(f^-, x_f(t)\right)}, \tag{18}$$

where signs "+" and "-" correspond to the values ahead and behind the shock front, respectively.

The linear stability condition of the front $x_f(t)$ is fulfilled (Gel'fand, 1959; Lax, 1973) if

$$f_s'\left(f^{-1}\left(x_f(t), f^+\right), x_f\right) < \frac{dx_f(t)}{dt} < f_s'\left(f^{-1}\left(x_f(t), f^-\right), x_f\right). \tag{19}$$

The Oleinik's admissibility condition (Gel'fand, 1959; Oleinik, 1959) for concave or convex FFFs follows from Lax's inequalities, Eq. (19).

4. Riemann solutions

Here, we consider solutions for various Riemann problems, including continuous solution for any convex FFF in Section 4.1, shock wave solution for any concave FFF in Section 4.2, transition from shock to continuous wave in Section 4.3, transition from continuous wave to shock in Section 4.4, and transport in periodical two-piece porous media in Section 4.5. Due to the vast variety of FFC forms encountered for liquid-gas flows in geological reservoirs, we investigate the exact Riemann solutions for various FFC shapes.

4.1. Continuous solution for convex FFF

Consider convex FFF with decreasing curvature in x, where curve II in Figure 1b reflects FFF at $x=0$, and curve I – at $x=1$. At $x=0$, occurs decay of the discontinuity in IC and BC by Eqs. (5, 6) in the Riemann solution, given by self-similar rarefaction wave:

$$s(x,t)=\begin{cases} 0, & 0<\dfrac{x}{t}<f_s'(0,0) \\ \dfrac{x}{t}=f_s'(s,0), & f_s'(0,0)<\dfrac{x}{t}<f_s'(1,0) \\ 1, & f_s'(1,0)<\dfrac{x}{t}<\infty \end{cases}. \tag{20}$$

Eq. (20) presents the asymptotic limit of the solution in the neighbourhood of origin. Figure 3b shows zoomed view of the characteristic lines in the vicinity of the origin. Extending the characteristic curves from $x=0$ results in a decrease in velocity for low f-values, where FFF slope f'_s decreases with x, and an increase in velocity for high f-values (see curves with $f=f^i$ and $f=f^k$ in Figure 3a). Indeed, the characteristic curve carrying value $f=0$ ($s=0$) is convex, while the curve with $f=1$ is concave. The implicit solution of the problem Eqs. (5, 6) is:

$$s(x,t)=\begin{cases} 0, & 0<t<\tau(x,0) \\ f^{-1}(f,x),\ t=\displaystyle\int_0^x \frac{dy}{f_s'\left(f^{-1}(f,y),y\right)}, & \tau(x,0)<t<\tau(x,1), \\ 1, & \tau(x,1)<x<\infty \end{cases} \tag{21}$$

where

$$\tau(x,0)=\int_0^x \frac{dy}{f_s'(0,y)},\ \tau(x,1)=\int_0^x \frac{dy}{f_s'(1,y)} \quad . \tag{22}$$

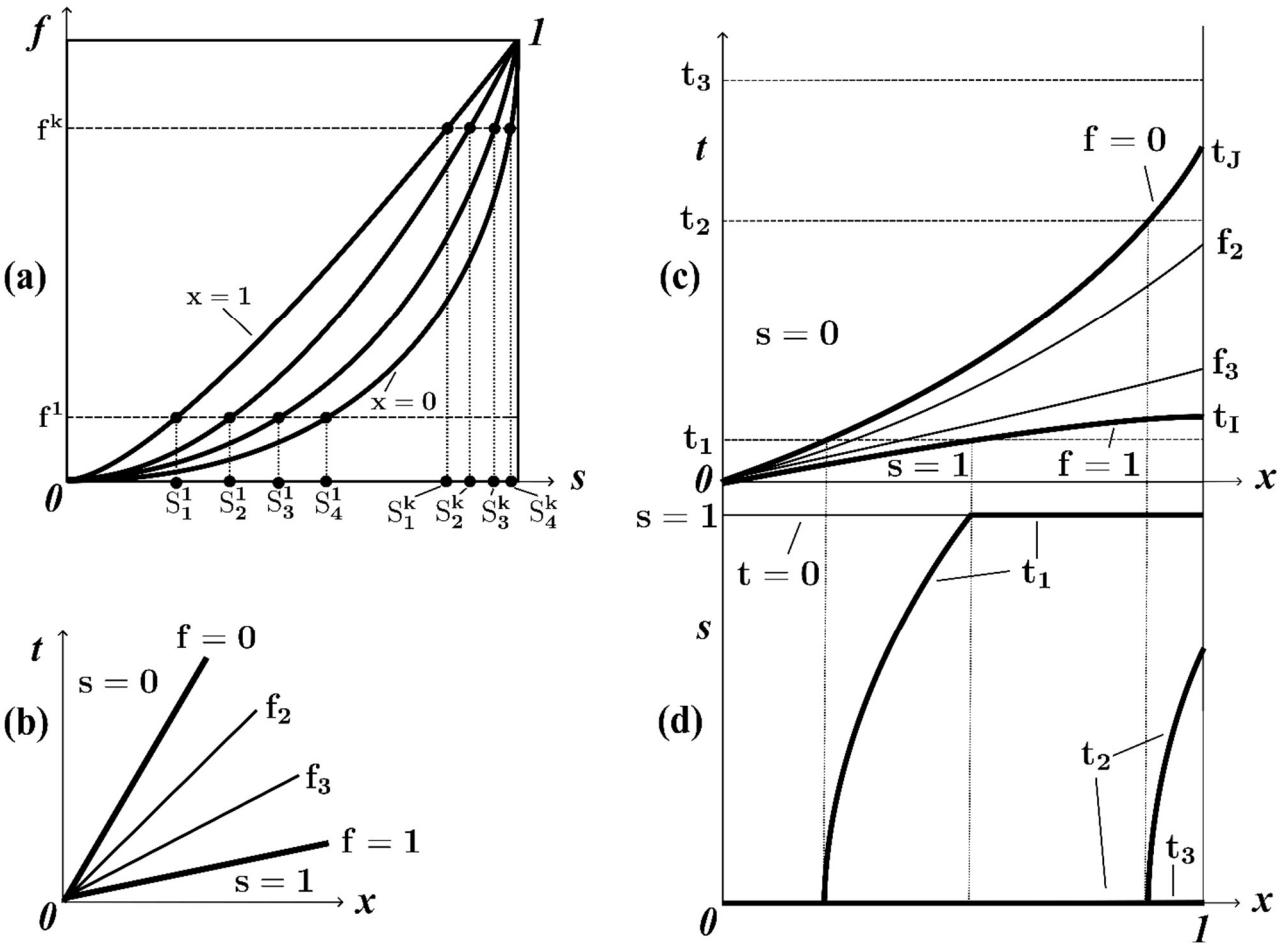

Figure 3. Exact solution for convex fractional flow curves FFCs (curves II and I from Figure 2 correspond to $x=0$ and $x=1$, respectively): a) convex FFCs with $f=f^I$ and $f=f^{II}$ and corresponding saturations for varying x; b) characteristic straight lines at $x<<1$ at the beginning of injection; c) characteristic lines for the overall domain $0<x<1$; d) saturation profiles in the moments t_1, t_2, and t_3.

Characteristics in zone $s(x,t)=0$ are obtained by the shift of the upper bound of the mixture zone $\tau(x,0)$ upwards by t_0. In zone $s(x,t)=1$, the characteristics are obtained by shifting the lower bound of the mixture zone $\tau(x,1)$ by such value that it crosses abscissa axes in point x_0. The equations for characteristics in these two distinct zones are

$$t = t_0 + \int_0^x \frac{dy}{f_s'(0,y)}, \quad t = \int_{x_0}^x \frac{dy}{f_s'(1,y)} \quad . \tag{23}$$

Figure 3c shows saturation profiles for four moments. The initial value corresponds to $t=0$. At the moment t_1, before the arrival of characteristic $f=1$ at the outlet $x=1$, $t_1<\tau(1,1)$, the profile contains the domain with $s=0$, the mixture zone, and the domain with $s=1$. After the arrival at the moment t_2, $\tau(1,1)< t_2<\tau(1,0)$, the profile consists of zones $s=0$ and the mixture zone. At the moment $t_3>\tau(1,0)$, the saturation profile is uniform with $s=0$.

With vanishing x-dependence of FFF (partial derivative of FFF by x tends to zero), the solution of Riemann problem Eq. (21) degenerates into self-similar solution Eq. (20).

Figure 4 presents the results of MATLAB calculations by Eq. (21) for the following x-dependent FFF

$$f(s,x) = \left[1 + \frac{k_{rgwi}(x)}{k_{rwgr}} \frac{(1-s)}{(s)} \frac{\mu_w}{\mu_g}\right]^{-1}, \quad \frac{k_{rgwi}(x)}{k_{rwgr}} = \left[k_{rgwi}(1) - k_{rgwi}(0)\right]x + k_{rgwi}(0). \tag{24}$$

Here the viscosity ratio is $\mu_w/\mu_g=33$, and the end point relative permeabilities $k_{rgwi}(0)=0.2$, $k_{rgwi}(1)=0.7$.

Figure 4a shows the convex fractional flow curves (FFC) for four x-values, Figure 4b – shows the characteristic curves for five f-values, and Figure 4c – shows four continuous curves for saturation profiles at four moments.

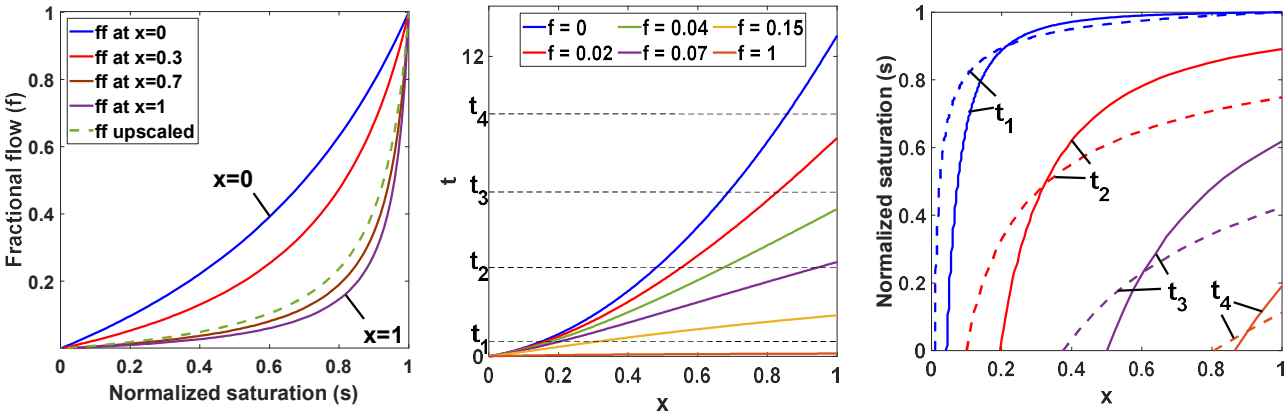

(a) (b) (c)

Figure 4. MATLAB calculations of exact solution for convex FFCs: (a) FFCs for four values of x; b) characteristic lines carrying six f-values; c) saturation profiles in four moments for microscale and upscaled models (continuous and dashed curves, respectively).

4.2. Shock wave solution for concave FFF

Concave FFFs in Figure 1b match the cases of the FFF change from curve IV at $x=0$ to curve V at $x=1$, or *vice versa*. The solution is given by the jump from 0 to 1, which propagated with unitary speed

$$s^+ = 1, \; s^- = 0, \; \frac{f(s^+,x) - f(s^-,x)}{s^+ - s^-} = 1. \tag{25}$$

Shock velocity in Eq. (25) is obtained from Hugoniot-Rankine condition of mass balance on the front, given by conservation law Eq. (2).

Ahead of the front, characteristics are given by Eq. (14) with $f(s,x)=1$. All characteristics are obtained from each other by shifting in the direction t and continue from axis x until intersecting with the shock front. Behind the front, characteristics are given by Eq. (15) with $f(s,x)=0$. Similarly, all characteristics are obtained from each other by shifting in direction t and continue from axes t until the intersection with the shock front. Figure 5 shows MATLAB calculations for FFF given by Eq. (24) and $k_{rgwi}(x)/k_{rwgr}=[0.02, 0.09]$, $\mu_w/\mu_g=5$. Figure 5a exhibits the forms of FFCs, Figure 5b – saturation profiles at four moments. The saturation microscale and upscaled profiles exhibit the same full-shock structure.

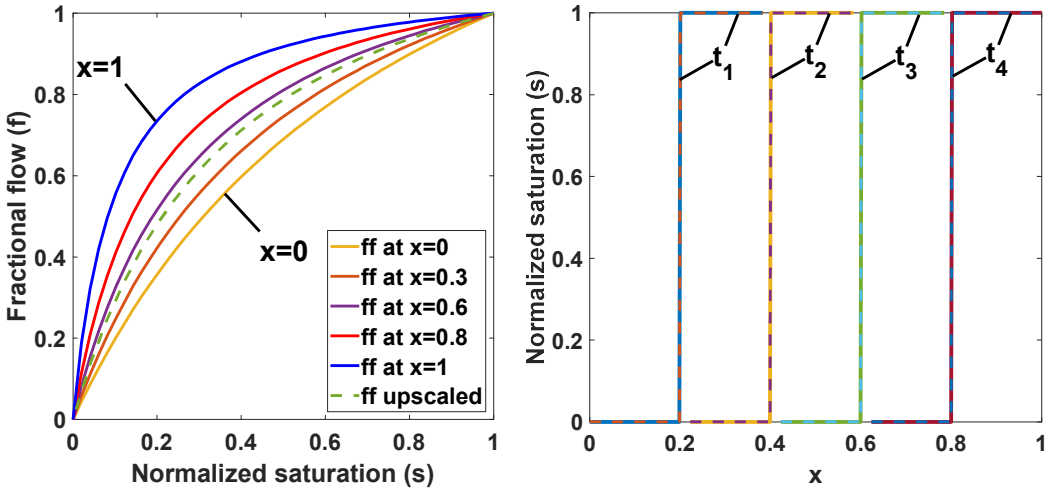

Figure 5. MATLAB calculations of the shock-wave solution for concave FFCs: (a) FFCs for micro and upscaled system (continuous and dashed curves respectively); (b) saturation profile at t_1, t_2, t_3, and t_4 for micro and upscaled systems.

4.3. Transition from shock to continuous wave with FFF decreasing in x from concave to convex

Consider the solution of the Riemann problem with FFF that is concave for $0<x<x_c$, is a straight line at $x=x_c$, and is convex for $x_c<x<1$. The examples for these FFCs are curves V, III, and I in Figure 1b, respectively.

The jump $0\rightarrow 1$ propagating with unitary speed is formed at the origin (Figure 6). This shock propagates until the moment $t=x_c$. From this moment on, the characteristics spread-out into the domain $t>x_c$, $x>x_c$. Like the solution given by Eqs. (20, 21), the behaviour of characteristics reflects decay of the discontinuity $0\rightarrow 1$, as shown in Figure 3b. The set of characteristics with the unitary speed starts at point (x_c, x_c) and carries all f-values with f varying from zero to one. Saturation distributions along characteristics are given by Eq. (12). The exact solution is:

$$s(x,t)=\begin{cases} 0, & t>x,\ 0<x<x_c \\ 1, & t<x,\ 0<x<x_c \\ f^{-1}(f,x),\ t=\int_{x_c}^{x}\dfrac{dy}{f_s'\left(f^{-1}(f,y),y\right)} & \tau_c(x,1)<t<\tau_c(x,0),\ x_c<x<\infty \\ 0, & \tau_c(x,0)<t<\infty,\ x_c<x<\infty \\ 1, & 0<t<\tau_c(x,1),\ x_c<x<\infty \end{cases}, \qquad (26)$$

where the upper and lower bounds for the mixture zone are

$$\tau_c(x,0)=x_c+\int_{x_c}^{x}\frac{dy}{f_s'(0,y)},\quad \tau_c(x,1)=x_c+\int_{x_c}^{x}\frac{dy}{f_s'(1,y)}. \qquad (27)$$

Saturation profiles are presented in Figure 6 at four moments: t_1 before the FFF transition from convex to concave ($t_1<x_c$), t_2 - before the arrival of the forward mixture front, ($t_2<\tau_c(1,1)$), t_3 - during mixture production, ($\tau_c(1,1)<t_2<$

$\tau_c(1,0)$), and t_4 after the arrival of the rear mixture front, ($t_4>\tau_c(1,0)$). The profile at the moment t_1 is full shock and it is smoothed up at the moment t_2.

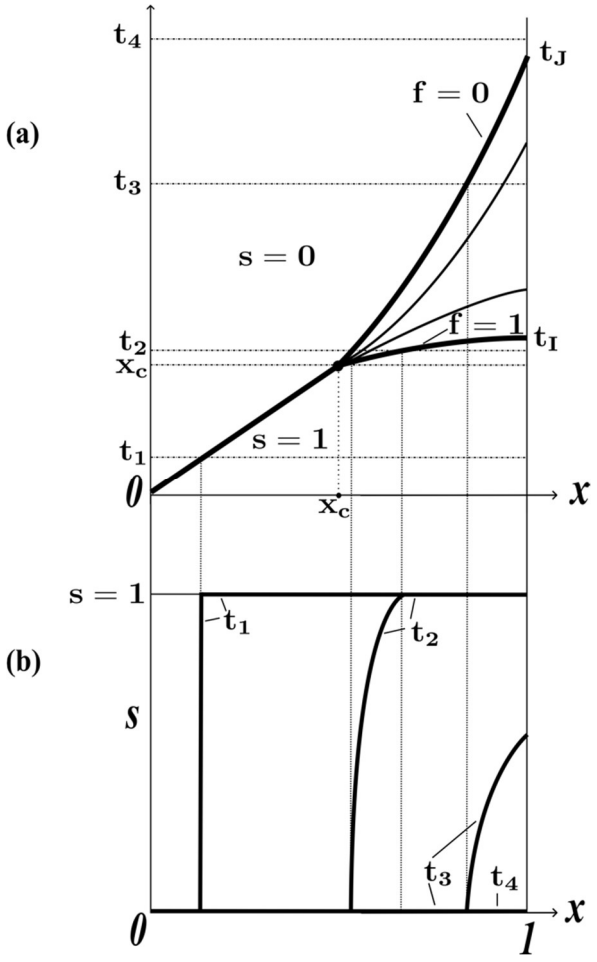

Figure 6. Displacement of water by gas for concave FFC at $x=0$ and convex at $x=1$ (curves IV and I from Figure 2) – transition from shock wave to rarefaction: a) shock trajectory and characteristic lines; b) saturation profiles at four moments t_1, …, t_4.

4.4. Transition from continuous wave to shock with FFF increasing in x from convex to concave

Consider FFF that corresponds to curve I in Figure 1b at $x=0$ and curve V at $x=1$. At the origin occurs the decay of discontinuity $0\rightarrow 1$ with self-similar configuration given by Eq. (20). The characteristics carrying values $f=0$ and $f=1$ are extended further from the origin in the first quadrant, where $x>0$, $t>0$ in the (x,t)-plane. As it follows from the forms of FFCs I and IV, the speed of characteristic $f=0$ increases with time, while the speed of characteristic $f=1$ decreases. These two curves intersect at the origin and at the point M (dashed curves in Figure 7); those two curves are called the envelope. Integrating both sides of Eq. (2) over the area bounded by the envelope and calculating the contour integral in Eq. (2) yields $x_M=t_M$. Figure 7 also shows the characteristics for f varying from zero to one. At $x=x_c$, the speeds of all characteristics are equal to one. All characteristics cover the envelope for $0<x<x_c$ and do not intersect inside it. The equations of characteristics here are Eq. (14) with $x_0=0$. This equation defines the arrival time at $x=x_c$ for each f-characteristic, as well as saturation $s_c(t)$ along the line $x=x_c$.

Along the straight-line $x=x_c$, characteristic speed is equal to one. Along the straight line $x=x_c+\varepsilon$, where $\varepsilon<<1$, the characteristic speed decreases from the moment $\tau(x_c+\varepsilon,1)$ from the value $f'_s(1, x_c+\varepsilon)$ until some moment $t_c(\varepsilon)$, and further decreases to the value $f'_s(1, x_c+\varepsilon)$ at the moment $\tau(x_c+\varepsilon,0)$. The characteristics start intersecting each other at the moment $t_c(\varepsilon)$ yielding the appearance of the shock that propagates along the trajectory $x=x_f(t)$. The moment t_c of appearance of the shock front is defined as the limit of $t_c(\varepsilon)$ as ε tends to zero:

$$t_c = \lim_{\varepsilon\to 0} t_c\left(x_c+\varepsilon\right) \quad . \tag{28}$$

Eq. (28) determines the starting point of the front $x=x_f(t)$:

$$x_f\left(t_c\right)=x_c. \tag{29}$$

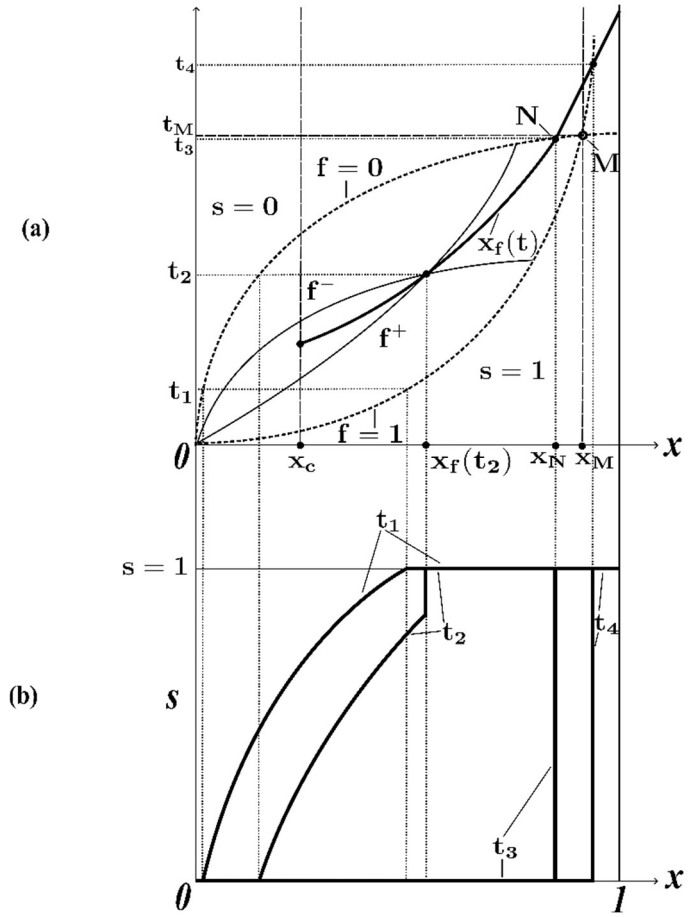

Figure 7. Exact solution for displacement of water by gas for convex FFC at $x=0$, straight line at $x=x_c$, and concave at $x=1$ (curves I, III, and V from Figure 2, respectively) – transition from rarefaction to shock wave: a) shock trajectory and characteristic lines; b) saturation profiles at four moments t_1, t_2, t_3, and t_4.

Consider any moment $t>t_c$, where the f-values ahead and behind the front at this moment t are $f^+(t)$ and $f^-(t)$ respectively. Both characteristics intersect at the point $(x_f(t), t)$. The saturation distributions along the characteristics carrying the values $f^+(t)$ and $f^-(t)$ follow from Eq. (12):

$$s=f^{-1}\left(x,f^-\right),\ \ s=f^{-1}\left(x,f^+\right), \tag{30}$$

respectively.

As it follows from Eq. (14) for characteristics

$$t=\int_0^{x_f(t)}\frac{dy}{f_s'\left(f^{-1}\left(y,f^-\right),y\right)}=\int_0^{x_f(t)}\frac{dy}{f_s'\left(f^{-1}\left(y,f^+\right),y\right)}\quad . \tag{31}$$

That is,

$$\tau\left(x_f\left(t\right),f^-\right)=\tau\left(x_f\left(t\right),f^+\right). \tag{32}$$

The ODE for shock speed follows from Hugoniot-Rankine condition of mass balance on the front, given by conservation law Eq. (2):

$$\frac{dx_f(t)}{dt} = \frac{f^+(t) - f^-(t)}{f^{-1}\left(x_f(t), f^+\right) - f^{-1}\left(x_f(t), f^-\right)}. \quad . \tag{33}$$

Expressing $f^-(x_f)$ and $f^+(x_f)$ at the moment t from Eq. (31) and substituting the results into the RHS of Eq. (33) yields an ODE with initial data defined by Eq. (29). The ODE, Eq. (33) allows for first integral. Let us integrate both sides of Eq. (2) over the domain Ω in the plane (x,t) limited by characteristics carrying the f-values, $f^-(x_f)$ and $f^+(x_f)$. Calculating the double integral of both sides of Eq. (2) over the domain Ω using Green's theorem:

$$0 = \iint_{\Omega} \left[\frac{\partial s}{\partial t} + \frac{\partial f(s,x)}{\partial x} \right] dxdt = \oint_{\Gamma} f dt - s dx = 0 \quad . \tag{34}$$

Accounting for the constancy of f along the characteristics and for Eq. (34), contour integral in (34) yields

$$f^- t - \int_0^{x_f(t)} f^{-1}\left(y, f^-\right) dy = f^+ t - \int_0^{x_f(t)} f^{-1}\left(y, f^+\right) dy. \tag{35}$$

Which is the first integral of the ODE, Eq. (33). Finally, the system of three transcendental equations Eqs. (31,35) for each $t>t_c$ defines three unknowns $f^-(t)$, $f^+(t)$, and $x_f(t)$.

Lax's stability condition, as expressed in Eq. (19), governs the arrival of two characteristics, which carry the values $f^-(t)$ and $f^+(t)$ on the front $x_f(t)$. The integration of the differential form (34) along the closed contour formed by the two characteristics within the intervals of the x and t axes, where BC and IC are set, yields the first integral of ODE for the front trajectory $x_f(t)$.

The trajectory $x_f(t)$ is shown in Figure 7. The trajectory leaves the envelope at the moment t_3, after intersecting the characteristic curve carrying $f=0$. In this case $s^-=f^-=0$, and system of three equations Eqs. (31,35) determines three unknowns t_3, $x_f(t_3)$, and $f^+(t_3)$. In this case, further behaviour of front $x_f(t)$ is defined by system (31,35) with the values behind the front $f^-=0$ and $f^{-1}(x, f^-)=0$. This occurs until the front intersects with the characteristic carrying $f=1$. The time of intersection is defined by Eq. (35) with $f^-=0, f^+=1$. Further, the values $f^-=0, f^+=1$ are maintained, and the front propagates with unitary speed.

If the trajectory $x_f(t)$ first intersects with the envelope characteristic carrying $f=0$ at the moment t_3, then $f^-=0$. The system of three transcendent equations Eqs. (31,35) determines three unknowns t_3, $x_f(t_3)$, and $f^+(t_3)$. The front first interacts with the wave of f-characteristic ahead of the front. In this case, further behaviour of front $x_f(t)$ is defined by system Eqs. (31,35) with $f^-=0$ and $f^{-1}(x, f^-)=0$. The time of intersection of the front with the characteristic carrying $f=1$ is defined by Eq. (35). Further, $f^-=0, f^+=1$, and the front propagates with unitary speed.

Figure 7 shows the saturation profiles at four moments. The solution transforms from a continuous profile at the moment t_1 into a full shock at the moment t_4.

In the particular case of FFFs, where the characteristic carrying f_1 propagate with velocity equal to one, i.e.,

$$f(s,x) = f_1, \; f_s'(s,x) = 1, \tag{36}$$

the trajectory of this characteristic is $x=t$, and it crosses point M. All characteristics carrying values $f<f_1$ are concave; all characteristics carrying $f>f_1$ are convex. The moment of initiation of the front $x_f(t)$ occurs at $t_c=x_c$.

4.5. Flow in periodical two-piece porous media

Consider two-phase flow in composite porous media shown in Figure 8a and 9a. Blue and red FFCs in Figure 8b correspond to the white and grey sections of the porous media with weights α and $1-\alpha$, respectively. As it follows from Hugoniot-Rankine condition in Eq. (33), at immobile shocks $x=x_k$, water flux is continuous: $f^-=f^+$. So, at $x=x_k$, where a rock-property change occur, i.e FFFs $f(s,x)$ are discontinuous, f-values are continuous; therefore, the saturation profiles are discontinuous:

$$f_\alpha\left(s^-, x_k\right) = f_{1-\alpha}\left(s^+, x_k\right),\ k = 1, 2\ldots. \tag{37}$$

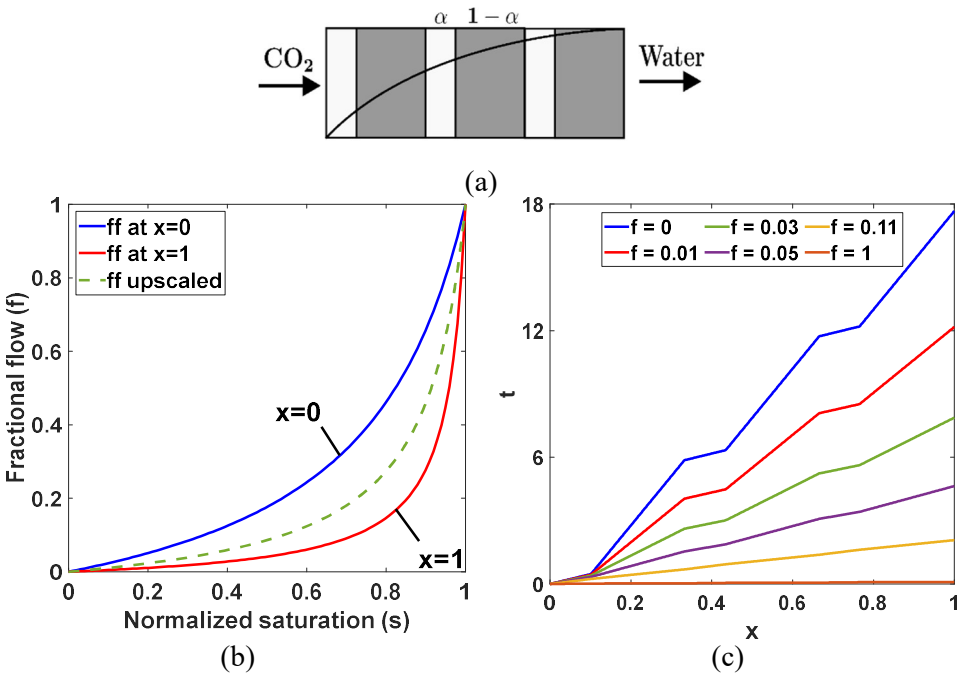

Figure 8. Two-phase flow in the porous media with piecewise-constant heterogeneity: a) schematic for periodical two-piece porous media (configuration 1); b) fractional flow curve for micro and upscaled system (continuous and dashed curves, respectively); (c) characteristic curves carrying six *f*-values for continuous solution.

In this case, the technique developed in this work yields the exact solutions obtained by Subramanian et al. (1999). Six characteristic lines in Figure 8c carry different *f*-values. The saturation profiles are discontinuous; the saturation shocks occur at the positions where the rock changes its properties (Figure 10). The initial saturation $s=1$ decreases to the profile at the moment t_1. Further displacement yields the shift of the profile in the direction of the flow (the profile at the moment t_2).

The composite porous media in Figure 9a consists of the same pieces as that in Figure 8a, except the sections are arranged in a different order. The FFCs in Figure 9b as well as characteristics in Figure 9c show changes in their order. Figure 10 presents the saturation profiles at two moments. The continuously shifting profiles in the direction of displacement changes the initial profile $s=1$ to $s=0$ at the end of displacement.

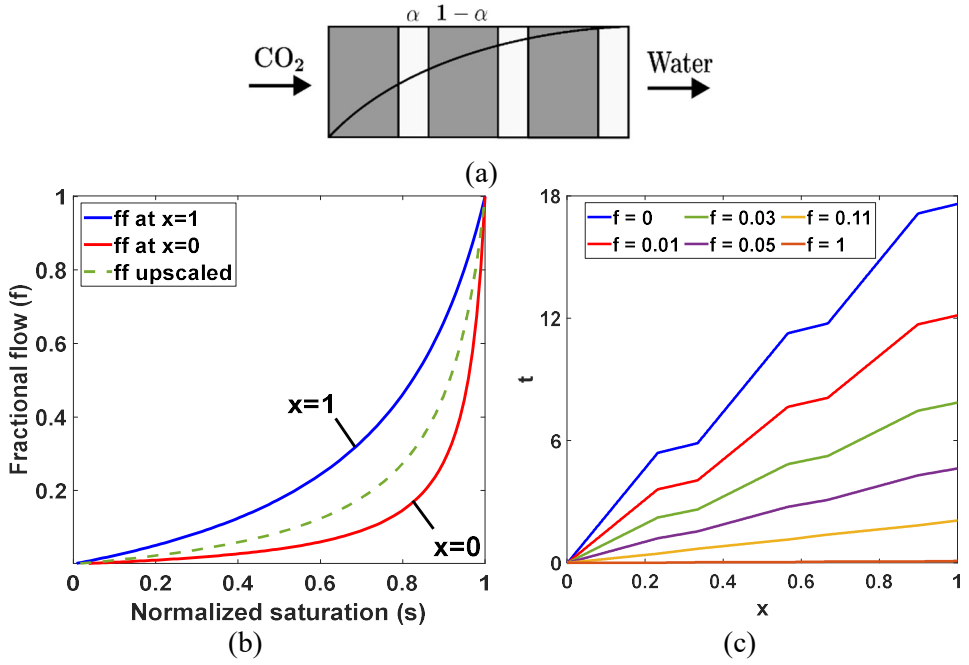

Figure 9. Effects of the order of homogeneous parts in periodical two-piece porous media: a) schematic for the porous media with two-piece periodical heterogeneity (configuration 2); b) FFCs for micro and upscaled system (continuous and dashed curves, respectively); (c) characteristic curves carrying six *f*-values for continuous solution.

Figure 10 compares the saturation profiles for the two composite porous media at the moments t_1 and t_2. Changing the order – switching grey to white and vice versa – results in significant change of saturation profiles.

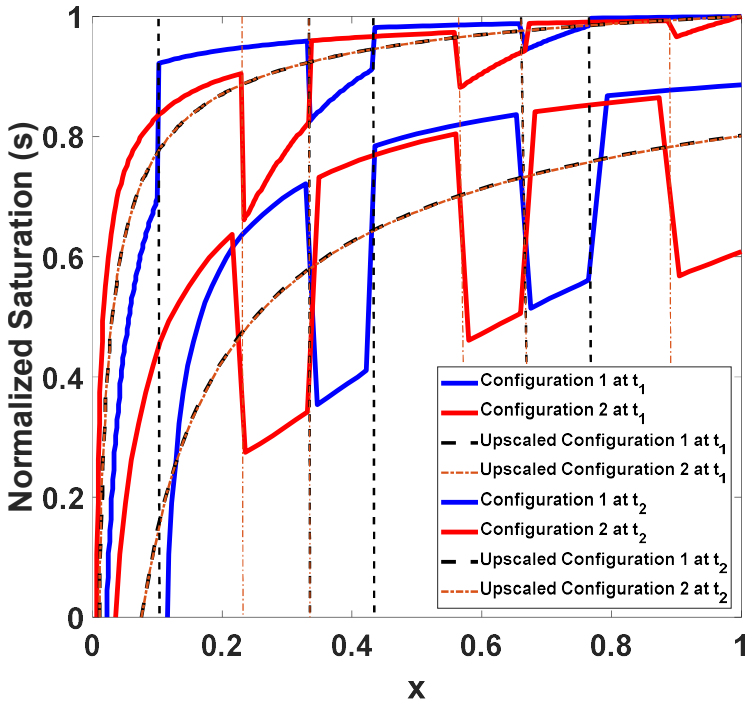

Figure 10. Comparison between micro-scale and upscaled saturation profiles for two-piece heterogeneous rocks with different order of homogeneous sections. Saturation profiles of piecewise constant configuration 1 (blue) and configuration 2 (red) with their corresponding upscaled saturation profile (black and brown respectively) at moments t_1 and t_2.

5. Exact continuous solution for non-Riemann initial-boundary value problem

Any arbitrary continuous solution of the initial-boundary value problem Eqs. (3, 4) is given by Eqs. (14,15), where characteristics carrying constant *f*-values are given in implicit form. The equations for characteristics Eq. (14) and Eq. (15) spread the initial and boundary *f*-values, respectively, within first quadrant $x>0$, $t>0$ of the (x,t) plane. The solution is

$$s(x,t)=\begin{cases} f^{-1}\left(f\left(s_0(x_0),x_0\right),x_0\right),\ t=\int_{x_0}^{x}\dfrac{dy}{f_s'\left(f^{-1}\left(f\left(s_0(x_0),x_0\right),y\right),y\right)}, & t<\tau\left(x,f_0(0)\right) \\ f^{-1}\left(f_0(t_0),x\right),\ t=t_0+\int_{0}^{x}\dfrac{dy}{f_s'\left(f^{-1}\left(f_0(t_0),y\right),y\right)}, & t>\tau\left(x,f_0(0)\right) \end{cases} . \qquad (38)$$

Figure 11 shows the characteristics where the Riemann initial-boundary value data $0\longrightarrow 1$ are continuously smoothed from zero *f*-value at $x=0$ and t tending to infinity, to $f_0(0)$ at $t=0$, $x=0$, and then along $t=0$ until $s=1$ at t tending to infinity. Here the solution is defined for $t>0$, $0<x<1$. In the area influenced by the boundary conditions, *f*-values vary $0<f<f(t_0)$. In the area of influenced by the initial conditions, *f*-values vary according to $f(s_0,0)<f<1$.

The exact solution, Eq. (38) for any heterogeneity $f(s,x)$ is a limit of solutions for flow in piecewise homogeneous rocks, i.e. $F=F_k(S)$ for the intervals $[x_0,x_1]$, $[x_1,x_2]\ldots[x_k,x_{k+1}]\ldots$, where $x_0=0$, $x_0<x_1,x_2\ldots x_n=1$ (Figure 2). The two-phase displacement within each homogeneous core is governed by Eq. (1), where constant S-values propagate along the characteristics with speed $F_k'(S)$. Thus, fractional flow $F=F_k(S)$ is also constant along the characteristics. As it follows from phase mass balance and incompressibility, the flux F is continuous at the borders $x=x_k$, $k=1,2\ldots n$, where the rock properties change by jumps. Consider the characteristic carrying value $s=S_1$, *or* $F_1=F(S_1)$ in the first

core; the propagation speed is equal to $F'(S_1)$. The saturation ahead of the first boundary S_2 between first and second cores is determined by the continuity of flux, $F_1(S_1)=F_2(S_2)$. The saturation S_2 and corresponding flux, F_2 propagate along characteristic with speed $F'(S_2)$ in the second core, and so on. Tending the number of cores N to infinity along with tending all lengths x_{k+1}-x_k to zero yields the characteristic form for flow in heterogeneous core, Eq. (11).

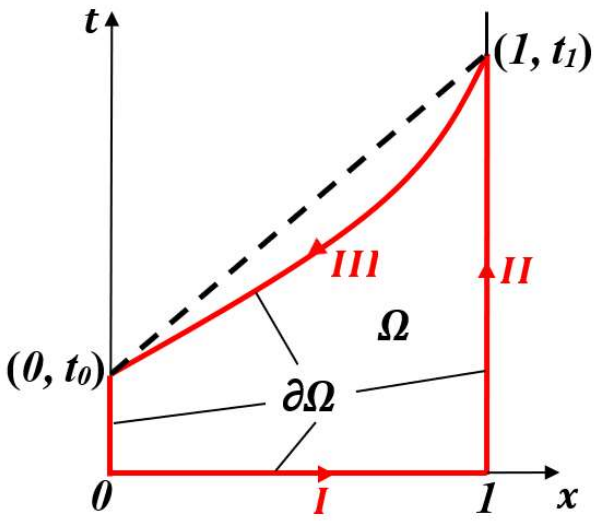

Figure 11. Upscaling procedure for continuous solution of initial-boundary-value problem

6. Upscaling of micro scale flow system and fractional flow curve

Here, we define upscaling based on production history (Section 6.1), saturation profile (Section 6.2), and their combination (Section 6.3). These three definitions are equivalent.

6.1. Upscaling based on production history

The definition of FFF upscaling from micro-scale heterogeneous $f(s,x)$ to upper scale $F(S)$ is as follows. For 1D flow problem, rock heterogeneity induces x-dependency of fractional flow function: $f=f(s,x)$, while the upscaled system is uniform: $F=F(S)$. The upscaling of micro-scale heterogeneous $f(s,x)$ involves determining a function $F(S)$ that preserves mass balance, i.e., has the same instantaneous or cumulative production at the outlet, $x=1$ for each moment $t>0$ as the micro-scale system, expressed by Eq. (7). The production $f_1(t)$ at the outlet $x=1$ is the same for microscale and upscaled models defined by Eq. (2) and Eq. (1), respectively.

The calculations are similar to Welge's method, which determines the fractional flow from the laboratory measurements of the outlet water-cut (Welge, 1952). Here we apply the extended Welge's technique to an exact continuous solution of micro-scale equation Eq. (1).

Consider the case where $t>\tau(1,f_0(0))$ and domain Ω bounded by curvilinear tetrahedron $\Gamma=\partial\Omega$: $(0,0)\rightarrow(1,0)\rightarrow(1,t)\rightarrow(0,t_0)\rightarrow(0,0)$ where $f=const$ along the side $(0,t_0)\rightarrow(1,t)$ (Figure 11). The calculation of the double integral of both sides of Eq. (2) over the domain Ω using Green's theorem defined in Eq. (34).

Integrals over the contours $(0,0)\rightarrow(1,0)$, $(1,0)\rightarrow(1,t)$, $(1,t)\rightarrow(0,t_0)$ and $(0,t_0)\rightarrow(0,0)$ are equal to

$$-\int_0^1 s_0(x,0)dx,\quad \int_0^t f_1(y)dy,\quad -f_1(t)t+\int_0^1 f^{-1}(f_1(t),x)dx,\quad -\int_0^{t_0} f_0(y)dy, \tag{39}$$

respectively. Here

$$t=\tau\left(f_0(t_0),1\right),\ f_1(t)=f_0(t_0). \tag{40}$$

The sum of the integrals over the contours is equal to zero. The averaged saturation in Eq. (39) is equal to $F^{-1}(f_1(t))$. Equalising the total of four components in Eq. (39) to zero yields the expression for averaged saturation:

$$S(1,t) = F^{-1}\left(f_1(t)\right) = \int_0^1 f^{-1}\left(f_1(t), x\right) dx = \int_0^{t_0} f_0(y)\, dy - \int_0^t \left(f_1(t) - f_1(y)\right) dy + \int_0^1 s_0(x,0)\, dx \quad . \tag{41}$$

The contour integral of differential form *fdt-sdx* over the contour $\partial\Omega$ is equal zero. Now consider the straight-line tetrahedron with the same vertex – $\partial\Omega$: $(0,0) \rightarrow (1,0) \rightarrow (1,t) \rightarrow (0,t_0) \rightarrow (0,0)$. The contour integral of differential form *Fdt-Sdx* over contour $\partial\Omega$ is also equal to zero. For Eq. (1), F is constant along straight line $(0,t_0) \rightarrow (1,t)$.

For differential forms *Fdt-Sdx* and *fdt-sdx*, the integrals over the contour $(0,0) \rightarrow (1,0)$ are equal due to the same ICs; over the contour $(1,0) \rightarrow (1,t)$ they are equal because the outlet flux $f_1(t)$ is the same; and over the contour $(0,t_0) \rightarrow (0,0)$ they are equal because the BCs are the same. Therefore, the integral of differential form *fdt-sdx* along the curvilinear characteristic $(0,t_0) \rightarrow (1,t)$ is equal to the integral of *Fdt-Sdx* along the straight-line characteristic $(0,t_0) \rightarrow (1,t)$, carrying the same *f*-value $f_0(t_0)=f_1(t)$:

$$f_0(t_0)\, t - \int_0^1 f^{-1}\left(f_0(t_0), y\right) dy = Ft - F^{-1}(F), \;\; F = f_0(t_0). \tag{42}$$

From the equality given by Eq. (7), it follows that upscaled saturation $S=F^{-1}(F)$ is equal to averaged saturation along the characteristic carrying the same *f*-value $f_1(t)$:

$$F^{-1}(f) = \int_0^1 f^{-1}(f, y)\, dy \,. \tag{43}$$

So, the upscaled FFF $F(S)$ corresponds S which is the averaged saturation along the characteristic line of the microscale model that carries the same *f*-value. In other words, in the inverse function to the upscaled fractional flow, saturation is obtained by averaging of the microscale saturation over the linear coordinate (x).

For the case where $t < \tau(x, f_0(0))$, we determine the contour integrals of the differential form *fdt-sdx* for Eq. (2) along the curvilinear triangle and *Fdt-Sdx* for Eq. (1) along the straight-line triangle defined by the vertex: $(x_0,0) \rightarrow (1,0) \rightarrow (1,t) \rightarrow (x_0,0)$. Both integrals are equal to zero. The integrals of both differential forms along straight line $(x_0,0) \rightarrow (1,0)$ are equal because the ICs are the same. The integrals along $(1,0) \rightarrow (1,t)$ are equal because $f(1,t)$ and $F(1,t)$ are equal to the same value $f_1(t)$. Therefore, the integral of differential form *fdt-sdx* along the curvilinear characteristic $(0,t_0) \rightarrow (1,t)$ is equal to integral of *Fdt-Sdx* along the straight-line characteristic $(0,t_0) \rightarrow (1,t)$, carrying the same *f*-value $f_0(t_0)=f_1(t)$. This equality is expressed by Eq. (42).

Figure 4 shows the form of x-dependent and upscaled FFFs by continuous and dashed curves, respectively, for continuous solution presented in Section 3.1. Figure 5 shows the form of x-dependent and upscaled FFFs by continuous and dashed curves, respectively, for shock solution presented in Section 3.2.

The upscaled equation Eq. (2) has the form of Eq. (1), where $F(S)$ is obtained from $f(s,x)$ by formulae given as Eqs. (43). The solution of upscaled Riemann problem for Eq. (1) is self-similar and given by Eq. (7). One-dimensional and quasi 1D problems for corefloods or injection in layer-cake reservoirs where pseudo-functions can be applied, are the Riemann problems, with $x_0=t_0=0$.

Solutions for upscaled model, where microscale FFCs vary from blue curve at $x=0$ to violet curve at $x=1$, are given in Figure 4 by dashed lines. Dashed FFC in Figure 4 is obtained by averaging the values $f^{-1}(f,x)$ in x and, therefore, is located between the blue and violet curves. Comparing with the microscale model, the upscaled model overestimates saturations closer to injection well, and underestimate saturations further away.

As Figure 4 shows, FFF for the microscale system decreases along x, and the dashed curve is located between the two boundary curves. Figure 4 shows that gas saturation $s_g=1-s$ predicted by the upscaled model is lower for small x and is higher for large x. Thus, the upscaled model forecasts a lower pore volume subjected to CO_2 capture near to well, and a higher pore volume farther from the well. Lower CO_2 saturation yields lower permeability damage due to salt precipitation and fines migration. The occurrence of formation damage near the well occurs increases the skin. So, underestimation of the formation damage near to well is not compensated by its overestimation farther

from the well. Therefore, underestimation of CO_2 saturation by the upscaled model yields underestimation of the well injectivity damage.

Figure 5 presents the upscaled FFF shown by the dashed curve; it is also located between those for $x=0$ and $x=1$. Yet, full-jump solutions – saturation profiles - for micro- and large scale in Figure 5 are the same. Therefore, for concave FFCs, the predictions of the behaviour of microscale and upscaled systems are the same.

Consider upscaling for the case of transition from shock to continuous wave with FFF decreasing in x from concave to convex (section 4.3, Figure 1b and 6). The governing equation (2) has first order, so no boundary condition is set at the outlet x=1. The initial-boundary value problem (2, 5, 6) is solved for x varying from x=0 at the inlet to x tending to infinity. Then, depending on core length L, the solution $s(x,t)$ is determined for $0<x<1$. Consider the case where $x_c>1$. Here, the solution is given by shock 0→1; FFCs vary from curve V to curve III in Figure 1b. Like in the case of shock-wave solution (section 4.2), the application of upscaling formula (43) yields concave FFF.

For the case x_c <1, all characteristics carrying constant f varying from zero to one, $0\le f\le 1$, converge at point $t=x_c$. The upscaled FFC, as obtained by formula (43), is a convex curve for $x>x_c$, and convex for $x<x_c$, like those in Figure 4a. This case shows that the upscaling result depends on the x_c value. Besides, upscaled FFF $F(S)$ depends on the size of the flow domain L.

In the case of transition from continuous wave to shock with FFF increasing in x from convex to concave (section 4.4, Figure 7), the upscaled FFC for $x_c>1$, where the straight-line x=1 is located to the left of $x=x_c$, is a convex curve like that in Figure 4a. For $x_N<1$, where the straight-line x=1 is located to the right of $x=x_c$, the solution is given by the shock 0→1, and the application of upscaling formula (43) yields concave FFF, like that in section 4.2, Figure 5. The cases $x_c<1<x_N$ and $x_N<1<x_M$ correspond to the combination of two above mentioned cases of upscaled FFCs. Here the upscaling result $F(S)$ also depends on x_c, x_N, x_M, and L.

Consider the two composite cores consisting of two homogeneous facies, marked in Figure 8a by white and grey. The same facies with the same fractions are arranged in Figure 9a in different order. So, the blue or red FFC in Figure 8 is the same as red or blue FFC in Figure 9, respectively. Applying the upscaling formula Eq. (43) yields

$$F^{-1}(f)=S(F,x)=a\,f^{-1}(F,0)+(1-a)\,f^{-1}(F,0). \qquad (44)$$

So, for a fixed f-value, the upscaled saturation is the arithmetic average of the values from the boundary curves, i.e., $f^{-1}(f,0)$ and $f^{-1}(f,1)$. Therefore, the dashed curves in both figures are equal. Figure 8c and Figure 9c show the characteristics carrying six different f-values. Formula (44) is invariant to change of the order of sections in the core, so the upscaled FFFs for two configurations coincide.

Figure 10 shows the saturation distributions $s(x,t)$ in two moments t_1 and t_2 for configuration 1 (blue curves) and configuration 2 (red curves). From the mass balance of both phases at the points of porous media discontinuity follows that fractional flow $f(s,x)$ is continuous. Therefore, saturation is discontinuous at the joint core section points. While the micro-scale saturation profiles for the two configurations differ significantly, the upscaled profiles, given by dashed lines, coincide.

For two configurations, the upscaled breakthrough histories and saturation profiles coincide. Let us explain the phenomenon. Consider propagation of characteristic carrying value f=const via the overall core. The time of arrival of the characteristic at the outlet x=1 is the total of their propagations in two core sections. For configuration 1 (Figure 8a), the arrival time is

$$\tau(1,f)=\frac{\alpha}{f_s'\left(f_\alpha^{-1}(f)\right)}+\frac{1-\alpha}{f_s'\left(f_{1-\alpha}^{-1}(f)\right)} \qquad (45)$$

where f_α and $f_{1-\alpha}$ are FFFs for white and grey cores, respectively.

For configuration 2 (Figure 9a), we have

$$\tau(1,f)=\frac{1-\alpha}{f_s'\left(f_{1-\alpha}^{-1}(f)\right)}+\frac{\alpha}{f_s'\left(f_{\alpha}^{-1}(f)\right)} \tag{46}$$

So, for each f, the arrival times for the first and second configurations are equal, i.e. breakthrough productions (water cuts) are equal for both configurations. Upscaled FFFs for the two configurations are equal, so the upscaled saturation profiles in Figure 10 coincide.

This result can be extended to any random discrete variation $0<x_1<\ldots<x_n=1$ and $f=f_k(s,x)$, $k=1,2\ldots n$, such as occurring in a numerical simulation. The arrival time of piecewise-straight characteristic to the outlet $x=1$ is equal to total of times of passing through each core section $(x_{k+1}-x_k)[f'_{k,s}(s)]^{-1}$. Change the order of sections in the composite core yields the corresponding change of order of additives in the series, which does not change the total.

For this case of discrete variation of FFF, where $0<x_1<\ldots<x_n=1$ and the flux, $f=f_k(s)$, $k=1,2\ldots, n$, the formula (43) is significantly simpler. Consider saturation values $S_1, S_2,\ldots, S_n$ that correspond to fixed flux value f^i=const. The upscaled saturation value that correspond to $F^i=f^i$ is an averaged arithmetic:

$$S\left(F^i\right)=\sum_{k=1}^{n}\left(x_k-x_{k-1}\right)S_k^i,\ \ f_k\left(S_k^i\right)=F^i \tag{47}$$

Taking a dense sequence $F^i=f^i$ varying from zero to one allows upscaling of the sequence $f=f_k(s)$ yielding the overall FFF $F=F(S)$.

6.2. Upscaling based on saturation profile

Consider the saturation profile that is either measured after coreflooding at $t=T$ by CT or X-ray scanning or generated by numerical solution of Eq. (2). The upscaled FFF $F(S)$ for the micro scale FFF $f(s,x)$ is defined as that having the same saturation profile $s_1(x,T)$.

Consider domain Ω bounded by curvilinear triangle $\Gamma=\partial\Omega$: $(0,0)\rightarrow(0,T)\rightarrow(x,T)\rightarrow(0,0)$ where $f=const$ along the side $(1,T)\rightarrow(0,0)$. The calculation of the double integral of both sides of Eq. (2) over the domain Ω is determined by Green's theorem defined in Eq. (34). Integrals over the contours $(0,0)\rightarrow(0,T)$, $(0,T)\rightarrow(1,T)$, and $(1,t)\rightarrow(0,0)$ are equal to

$$\int_0^T f_0(y)\,dy,\quad -\int_0^x s(y,T)dy,\quad -ft+\int_0^1 f^{-1}(f,x)\,dx=-ft+\left\langle S(f,x)\right\rangle, \tag{48}$$

respectively. Equalising the total of the three components in Eq. (48) to zero yields the expression for saturation averaged along the characteristics with f=const $\langle S\rangle$:

$$\left\langle S(f,x)\right\rangle=\int_0^x s(y,T)dy-\int_0^T f_0(y)\,dy+f(x,T). \tag{49}$$

Here averaged saturation $\langle S\rangle$ is the same as that given by Eq. (30), meaning that $\langle S\rangle=F^{-1}(F)$.

6.3. Combined method for upscaling based on both water-cut and saturation profile

Consider coreflood occurring during the time $[0,T]$, when the minimum value $f=0$ has not been reached, with post-mortem measurement of saturation profile at $t=T$ and x varying from zero to one. Apply Eq. (41) while treating water-cut data $f_1(t)$ from $t=0$ to $t=T$. This provides $F(S)$ from the water-cut value varying from $f_1(T)$ and one. Applying Eq. (49) to treat saturation profile at $t=T$ delivers $F(S)$ varying from zero to the water-cut value at $x=1$ and $t=T$. So, water-cut-history based upscaling determines the FFF where F varies from $f_1(T)$ to one, and saturation-profile-based upscaling determines $F(S)$ from zero to $f_1(T)$.

Consider CT scan with the frame moving along the trajectory $x_0(t)$ from $x=0$ to $x=1$ and back several times during coreflooding in heterogeneous core. The saturation $s(x_0(t))$ is measured along the trajectory. The integration using Eq. (34) allows the determination of the upscaled $F(S)$ from the minimum value $f(s(x_0(t)), x_0(t))$ to one.

7. Numerical models for micro-scale and upscaled systems

Let us perform the upscaling of FFF, $f(s,x)$ in intervals between node points $x_0, x_1 \ldots x_n$, resulting in FFFs $F_n(S)$, (Figure 2), where the two inverse functions:

$$f = F_n(s),\ s = f^{-1}{}_n(f),\ x \in [x_n, x_{n+1}],\ n = 0,1 \ldots N,\ x_0 = 0,\ x_N = 1. \tag{50}$$

are determined for each interval.

Let us demonstrate that the f-values for the microscale solution of IBV problem Eqs. (2-4) and the solution for upscaled problem with functions $F_n(S)$ coincide at the nodal points $x_0, x_1 \ldots x_n$:

$$f\left(s(x_k,t),x\right) = F_k\left(s(x_k,t)\right). \tag{51}$$

We use the method of induction and perform the upscaling using Eq. (43) in the interval $[x_0,x_1]$. By the definition of upscaling, for $k=0$, the equality $f(s(x,t)=F(S(1,t))$ holds at $x=x_1$. Now assume that $f(s(x,t)=F(S(1,t))$ for any $k>1$, i.e., the boundary condition Eq. (4) at $x=x_k$ for Eq. (2) and Eq. (51) is the same. By the definition Eq. (43), $f(s(x,t)=F(S(1,t))$ for $k+1$, which proves the equality given by Eq. (51) for any number of intervals.

The coincidence of FFCs of the microscale and upscaled systems can be applied to numerical reservoir simulation. In particular, the production of phases at the outlet, $x=1$, for both systems is the same for microscale and upscaled problems, i.e., it is independent of the node locations.

8. Discussions

For heterogeneous media, where $f=f(s,x)$, the flux f is Riemann invariant. In the particular case of homogeneous media with $f=f(s)$, the saturation s conserves along characteristics, so flux $f(s)$ also conserves, as it must be in more general case of a heterogeneous medium.

From the flux, f being Riemann invariant follows the exact solutions, in particular the formulae (14, 15) for characteristics. These formulae are implicit and require numerical integration to produce the results.

The mathematical model of 1D two-phase flow in heterogeneous formation involves x-dependent phase permeability, yielding FFF $f=f(s,x)$. A spatial absolute permeability distribution $k(x)$ is not used in the model (Appendix B).

The exact solutions for Buckley-Leverett equation with coordinate-dependent flux, derived in Sections 4 and 5, can be used (i) for significantly accelerated inverse solvers, where the exact solutions can be used for direct or forward runs, (ii) for coreflood modelling and the analysis of the results, (iii) for streamline prediction of field production related to two phase flow, (iv) as benchmarks for numerical simulation.

Composite core flooding: The production-history based upscaling reflects the laboratory coreflood where the effluent water-cut is measured to determine the FFF. Eqs. (41, 43) show that, for micro heterogeneous porous media, Welge's method determines upscaled FFF. The same corresponds to the production history generated numerically by solving microscale model Eq. (2) – Welge's method upscales FFF automatically.

The saturation-profile based upscaling reflect measurements by CT or X-ray technique during coreflooding. Eq. (51) determines upscaled FFF from saturation profile measurements. The same corresponds to the saturation profiles generated numerically by solving micro scale model (2) – Eqs. (43, 51) upscales FFF automatically.

The combined method reflects measurements of water-cut until moment T with the following postmortem saturation profile measurement. The water-cut data determine FFF from $f=1$ to $f_0(0)$ using Eqs. (42, 43), and saturation profile data determines FFF from $f_0(0)$ to zero using Eqs. (51).

Numerical reservoir simulation: The exact solutions presented in section 4 along with upscaling Eq. (43) can benchmark not only numerical schemas for solution of Eq. (2), but also numerical upscaling algorithms. In particular, Eqs. (43, 47) provide upscaling of FFF for flows perpendicular to reservoir layering. For a numerical model, where inverse function $s=f^{-1}(f,x)$ does not vary with x over each interval $[x_n,x_{n+1}]$, the upscaled inverse function $S=F^{-1}(F)$ is equal to the arithmetic average of the saturation values in the intervals, weighted by the lengths of each intervals $(x_{n+1} - x_n)$. This allows upscaling in Eq. (2) from dense numerical grid to a coarse grid.

For *streamline* reservoir simulation, mass balance of water along the streamline is expressed in terms of the stream-tube with varying cross section $A(x)$ (Thiele & Batycky, 2001; Thiele et al., 1996)

$$A(x)\frac{\partial s}{\partial t}+\frac{\partial\left[A(x)f(s,x)\right]}{\partial x}=0. \tag{52}$$

Here, the heterogeneity along streamlines $f(s,x)$ corresponds to crossing of different sedimentary layers by the streamlines. Introduction of stream-tube volume in Eq. (52)

$$z(x)=\int_0^x A(y)\,dy \tag{53}$$

transforms it to the form of Eq. (2). Eqs. (21, 26, 35) deliver exact solutions along the streamlines for different forms of FFFs. Formulae (50, 51) provide the exact upscaling along each streamline.

Upscaling formulae (43, 47) can extend the computing technique for phase saturation statistics from probabilistic absolute permeability distributions to those of phase permeabilities (Fuks et al., 2019; Yang et al., 2022).

Practical calculations Depending on the form in which FFF is given, either of the two following methods for calculating the production history at x=1 and saturation profile at $t=T$ can be applied.

Discretise f-interval as $f^1,\dots f^i,\dots$ and use the analytical microscale model. Eq. (14) with $x_0=0$ can be applied to calculate the arrival time tk that corresponds to f-value f^i. Otherwise, calculate the upscaled values S_i that correspond to $F^i=f^i$ using Eq. (43). The arrival time t_i is calculated from self-similar solution of the Buckley-Leverett equation (1), like the second formula in Eq. (20)

$$t_i=\frac{S_{i+1}-S_{i-1}}{F^{i+1}-F^{i-1}}, \tag{54}$$

yielding water-cut history (t_i,F^i), $i=1,2\dots$ at $x=1$. Saturation profile (x_i,S_i) at $t=T$ is also calculated using the self-similar Buckley-Leverett solution (20):

$$x_k=\frac{F_{k+1}-F_{k-1}}{S_{k+1}-S_{k-1}}t_0 . \tag{55}$$

Determining saturation profile (x_i,s_i) using microscale model involves solution of transcendental equation (14) with respect to unknown x_k for given f^k and T.

Upscaling of partly miscible flows: The upscaling technique given by Eqs. (41-43) can be applied to flow of partly miscible fluids, like water and CO_2. Consider water evaporation into CO_2 with equilibrium vapour concentration in gas, $c_w(p,\theta)$ and CO_2 dissolution in water with equilibrium CO_2 concentration in water, $c_g(p,\theta)$, where θ is the reservoir temperature and p is pressure. Consider single-phase and two-phase domains of the phase diagram in the space (C,p,θ), where C is water concentration in water-CO_2 mixture. In two-phase domain, where $c_w<C<1-c_g$, water

saturation varies from zero to one, and the water-flux function $U_c(C)$ is calculated using Eq. (B7) for FFF. In single-phase domain of oversaturated water where $C>1-c_g$, saturation exceeds one, and water flux is equal to water concentration in the binary mixture, yielding straight line $U_c=C$. In the single-phase domain of undersaturated gas where $C<c_w$, saturation is negative, and water flux is also equal to water concentration in the binary mixture, yielding straight line $U_c=C$ too. The curve for water flux, U_c versus C has traditional form in two-phase domain and two straight "horns" in single-phase domain (Bedrikovetsky, 1993; Wachmann, 1964). The mass balance equation has the form of conservation law Eq. (1) with FFF $U_c(C)$. In the general case, the solutions for displacement of oversaturated water by undersaturated gas includes the first shock from gas to two-phase fluid, and the second shock from two-phase fluid to oversaturated water. Micro heterogeneity can yield x-dependencies of phase permeability $K_w(S,X)$, $K_g(S,X)$ and component concentrations $c_g(p,\theta,X)$ and $c_w(p,\theta,X)$. Exact solutions from sections 3-5 and upscaling technique from section 6 can be applied for the cases where $U_c=U_c(C,X)$.

Extension to two-phase multicomponent flows: Consider large-scale approximation of two-phase n-component flow, where dissipative effects of capillary pressure, diffusion, and non-equilibrium interphase mass exchange are ignored. The introduction of Lagrangian coordinate as an independent variable instead of time t, splits the system into n mass balance single-phase equations for each component, and one equation for saturation (Borazjani & Bedrikovetsky, 2017; Borazjani et al., 2016). In many cases of rock-brine-gas equilibrium, the solution contains only constant component concentrations (Bedrikovetsky, 1993; Johns, 1992; Lake et al., 2014). In this case, like for Eq. (2), Riemann invariant is flux f, leading to analytical solutions and upscaling technique for two-phase n-component flows.

Effects of capillary pressure: Capillary pressure can highly affect coreflood data interpretation. The proposed upscaling technique, given by Eqs. (41-43), cannot be extended for the overall case where capillary pressure is accounted for. However, for composite cores with piecewise constant properties, like those discussed in section 4.5, the analytical solution can account for capillary pressure. Barenblatt et al. (1990) and Hussain et al. (2012) solve the displacement problem with capillary pressure by matching the singular asymptotic expansions. Here, the Buckley-Leverett solution is matched with the transition-zone travelling wave near the displacement front and with the steady-state end-point solution near to the core outlet. Matching the large-scale capillary-pressure-free solution with travelling wave can be performed for the displacement front moving throughout the overall composite core. The steady-state end-effect solution can be used near to all points of media property discontinuity, where the core sections are connected.

9. Conclusions

Exact integration of the first order conservation law with coordinate-dependent flux and its upscaling allow for the following conclusions.

For any initial-boundary value problem, the flux is Riemann invariant; the characteristics allow for first integral yielding implicit formulae for the characteristics. First integrals for front trajectories are obtained by integrating the differential mass balance form $f(s,x)dt-sdx$ over the closed contours in plane (x,t) that comprise two arriving characteristics f^- and f^+ and the intervals of the axes x and t where the initial-boundary values are given.

If for any x FFF remains convex, the solution of the Riemann problem with $s_I<s_J$ is continuous. The same occurs for concave FFF and $s_I>s_J$. If for any x FFF remains concave, the solution of Riemann problem with $s_L>s_J$ is given by a full jump or shock. The same occurs for convex FF function where $s_I<s_J$.

If FFF is concave for $x<x_c$, straight line at $x=x_c$ and convex at $x>x_c$, and $s_I<s_J$, the solution remains jump or shock while $x<x_c$, the front smoothens up at $x=x_c$ and continuous wave propagates further at $x>x_c$. If FFF is convex for $x<x_c$, a straight line at $x=x_c$ and concave at $x>x_c$, where $s_I<s_J$, the solution remains continuous while $x<x_c$, the front with zero jump appears at $x=x_c$ and propagates further at $x>x_c$ with increasing jump**.**

The method to upscale a microscale FFF $f(s,x)$ into large-scale FFF $F(S)$ is as follows. Saturation S that corresponds to upscaled value $F=F(S)$ is an average in x from zero to one of the "microscale" saturation $s=f^{-1}(f,x)$.

This upscaling formula for $F(S)$ is valid for three formulations of its determination for a given $f(s,x)$: (i) from the flux $f_1(t)$ at the outlet $x=1$; (ii) from saturation profile $s(x,T)$ for a fixed moment $t=T$; (iii) from the combined data of water-cut $f_1(t)$, $0<t<T$, and saturation $s(x,T)$, $0<x<1$.

The results of water-cut based upscaling depends on length L, while that of saturation-profile based upscaling depends on the time interval T. In particular, in numerical modelling using finite difference methods, these two upscaling methods depend on grid size and time step.

The numerical solution obtained by an explicit finite difference method with advance over Δx for microscale model, coincides with the solution for the large-scale system obtained by history-based upscaling, at the points on the numerical cell boundaries $x_0, x_1, \ldots, x_n$.

The Welge's method for determining fraction flow from water-cut during coreflooding, when applied to heterogeneous core with $f(s,x)$, yields the upscaled fractional flow function $F(S)$.

Acknowledgements

PB dedicates this work to golden memory of his mentor in mathematical physics Prof A M Vinogradov (Moscow Lomonosov State University). Many thanks are due to Prof Anthony Roberts (University of Adelaide) for encouraging discussions on upscaling. The research did not receive any specific grant from funding agencies in the public, commercial, or not-for-profit sectors. There are no data sharing issues in the paper.

Appendix A. Assumptions of the model

For one-dimensional two-phase flow, we assume phase immiscibility and incompressibility. The rock is undeformable. For each phase is assumed modified Darcy's law with saturation-dependent phase permeability. The phase permeability depends on linear coordinate along the flow direction at the micro scale and is independent of this coordinate at the large scale. Initial and residual saturations are constant. At large scale, capillary pressure is neglected when compared with phase pressures, i.e. pressure in both phases is the same.

These restrictions are valid at both scales. However, at low scale, viscous forces that are proportional to the typical length, can be comparable with capillary forces, while viscous forces dominate the capillary force at the upper scale. This restricts application of the developed upscaling technique to composite cores.

Appendix B. Derivation of governing equations

The governing system for 1D two-phase capillary-pressure-free flow in heterogeneous rocks consists of mass balance equations for water and gas

$$\phi\frac{\partial\rho_w\overline{S}}{\partial T}+\frac{\partial\rho_w U_w}{\partial X}=0\ , \tag{B1}$$

$$\phi\frac{\partial\rho_g(1-\overline{S})}{\partial T}+\frac{\partial\rho_g U_g}{\partial X}=0\ , \tag{B2}$$

and momentum-balance Darcy's equations for water and gas

$$U_g=-\frac{K_g(\overline{S},X)}{\mu_g}\frac{\partial P}{\partial X}\ , \tag{B3}$$

$$U_w=-\frac{K_w(\overline{S},X)}{\mu_w}\frac{\partial P}{\partial X}\ . \tag{B4}$$

Here $\overline{S}$ is the water saturation, ϕ is the porosity, indexes "w" and "g" correspond to water and gas phases, respectively, ρ_w and ρ_g are phase densities, U_w and U_g are phase velocities, K_w and K_g are the phase permeability, μ_w and μ_g are phase viscosities, P is the pressure.

Factoring out the constant phase densities in Eqs. (B1, B2) and adding the results yields

$$U = U_w + U_g = U(t), \tag{B5}$$

i.e., the total flux U depends on time alone.

Adding Eqs. (B3, B4) yields the expression for the total flux

$$U = -\left[\frac{K_w(\bar{S}, X)}{\mu_w} + \frac{K_g(\bar{S}, X)}{\mu_g}\right]\frac{\partial P}{\partial X}. \tag{B6}$$

Expressing pressure gradient from Eq (B6) and substituting into Eqs (B3-B5) result in the following expression for water flux

$$U_w = -\frac{K_w(\bar{S}, X)}{\mu_w}\frac{\partial P}{\partial X} = \frac{K_w(\bar{S}, X)}{\mu_w}\left(\frac{K_w(\bar{S}, X)}{\mu_w} + \frac{K_g(\bar{S}, X)}{\mu_g}\right)^{-1} U = f(\bar{S}, X)U, \tag{B7}$$

where $f(\bar{S},X)$ is called the fractional flow function FFF. Substitution of expression (B7) into mass balance equation (B1) results in one equation for unknown saturation $\bar{S}(X,T)$:

$$\phi\frac{\partial \bar{S}}{\partial T} + U\frac{\partial f(\bar{S}, X)}{\partial X} = 0. \tag{B8}$$

Let us introduce dimensionless variables and parameters:

$$x = \frac{X}{L},\ t = \frac{1}{\phi(1 - S_{gr} - S_{wi})L}\int_0^T U(y)dy,\ p = \frac{K_0 P}{\mu_w U(T) L},\ s = \frac{\bar{S} - S_{wi}}{1 - S_{gr} - S_{wi}}. \tag{B9}$$

Substitution of the dimensionless variables and parameters (B9) into Eq. (B8) results in Eq. (2) presented in the main body of the text. In the main text, the normalised water saturation, s is called saturation.

Nomenclature

Parameters

f	Fractional flow at micro scale	[-]
F	Upscaled fractional flow	[-]
K_o	Absolute permeability	[mD]
K_g	Effective permeability of gas	[mD]
K_w	Effective permeability of water	[mD]
L	Length of porous medium	[m]
P	Pressure	[Pa]
s	Normalized water saturation	[-]
S	Upscaled water saturation	[-]
s_I	Initial water saturation	[-]
s_J	Injected water saturation	[-]
$\bar{S}$	Water saturation	[-]
S_{gr}	Residual gas saturation	[-]
S_{wi}	Connate water saturation	[-]
t	Dimensionless time	[-]
T	Dimensional time	[s]
U	Total flux	[m/s]

U_g	Flux of gas	[m/s]
U_w	Flux of water	[m/s]
x	Dimensionless linear variable	[-]
X	Dimensional linear coordinate	[m]

Symbols

α	Density of rock type	[-]
ϕ	Porosity	[-]
μ_g	Gas viscosity	[Pa s]
μ_w	Water viscosity	[Pa s]
ρ_g	Gas density	[kg m^{-3}]
ρ_w	Water density	[kg m^{-3}]
τ	Time of arrival of characteristics	[-]

Abbreviations

1D	One-dimensional space
2D	Two-dimensional space
3D	Three-dimensional space
BC	Boundary condition
FFC	Fractional flow curve
FFF	Fractional flow function
IC	Initial condition
LHS	Left hand side
ODE	Ordinary differential equation
PDE	Partial differential equation
RHS	Right hand side

References

Anto-Darkwah, E., Benson, S., & Rabinovich, A. (2021). An improved procedure for sub-core property characterization using data from multiple coreflooding experiments. *International Journal of Greenhouse Gas Control*, *105*, 103226. https://doi.org/10.1016/j.ijggc.2020.103226

Barenblatt, G. I., Entov, V. M., & Ryzhik, V. M. (1990). *Theory of fluid flows through natural rocks* (Vol. 395). Springer.

Barker, J. W., & Dupouy, P. (1999). An analysis of dynamic pseudo-relative permeability methods for oil-water flows. *Petroleum Geoscience*, *5*(4), 385-394. https://doi.org/10.1144/petgeo.5.4.385

Barker, J. W., & Thibeau, S. (1997). A critical review of the use of pseudorelative permeabilities for upscaling. *SPE Reservoir Engineering*, *12*(02), 138-143. https://doi.org/10.2118/35491-PA

Bedrikovetsky, P. (1993). *Mathematical Theory of Oil & Gas Recovery*. https://doi.org/10.1007/978-94-017-2205-6

Bedrikovetsky, P., Osipov, Y., Kuzmina, L., & Malgaresi, G. (2019). Exact upscaling for transport of size-distributed colloids. *Water Resources Research*, *55*(2), 1011-1039. https://doi.org/10.1029/2018WR024261

Borazjani, S., & Bedrikovetsky, P. (2017). Exact solutions for two-phase colloidal-suspension transport in porous media. *Applied mathematical modelling*, *44*, 296-320. https://doi.org/10.1016/j.apm.2016.12.023

Borazjani, S., Behr, A., Genolet, L., Kowollik, P., & Bedrikovetsky, P. (2019). Ion-exchange inverse problem for low-salinity coreflooding. *Transport in Porous Media*, *128*, 571-611. https://doi.org/10.1007/s11242-019-01260-8

Borazjani, S., Roberts, A. J., & Bedrikovetsky, P. (2016). Splitting in systems of PDEs for two-phase multicomponent flow in porous media. *Applied Mathematics Letters*, *53*, 25-32. https://doi.org/10.1016/j.aml.2015.09.014

Bruining, H. (2021). *Upscaling of Single-and Two-Phase Flow in Reservoir Engineering*. CRC Press.

Buckley, S. E., & Leverett, M. (1942). Mechanism of fluid displacement in sands. *Transactions of the AIME*, *146*(01), 107-116. https://doi.org/10.2118/942107-G

Chen, Y., & Durlofsky, L. J. (2006). Adaptive local–global upscaling for general flow scenarios in heterogeneous formations. *Transport in Porous Media*, *62*, 157-185. https://doi.org/10.1007/s11242-005-0619-7

Chen, Y., & Li, Y. (2009). Local-global two-phase upscaling of flow and transport in heterogeneous formations. *Multiscale modeling & simulation*, *8*(1), 125-153. https://doi.org/10.1137/090750949

Cheng, K. B., & Rabinovich, A. (2021). Optimization-based upscaling for gravity segregation with 3D capillary heterogeneity effects. *Journal of Hydrology*, *603*, 127062. https://doi.org/10.1016/j.jhydrol.2021.127062

Chung, E., Efendiev, Y., & Hou, T. Y. (2023). Nonlinear non-local multicontinua upscaling. In *Multiscale Model Reduction: Multiscale Finite Element Methods and Their Generalizations* (pp. 413-438). Springer. https://doi.org/10.1007/978-3-031-20409-8_15

Dafermos, C. M. (1983). Hyperbolic systems of conservation laws. In *Systems of nonlinear partial differential equations* (pp. 25-70). Springer. https://doi.org/10.1007/978-94-009-7189-9_2

Darman, N., Pickup, G., & Sorbie, K. (2002). A comparison of two-phase dynamic upscaling methods based on fluid potentials. *Computational Geosciences*, *6*, 5-27.

Das, D., & Hassanizadeh, S. (2005). *Upscaling multiphase flow in porous media*. Springer. https://doi.org/10.1007/1-4020-3604-3

Datta-Gupta, A., & King, M. J. (2007). *Streamline simulation: theory and practice* (Vol. 11). Society of Petroleum Engineers.

Efendiev, Y., Gildin, E., & Yang, Y. (2016). Online adaptive local-global model reduction for flows in heterogeneous porous media. *Computation*, *4*(2), 22. https://doi.org/10.3390/computation4020022

Efendiev, Y. R., & Durlofsky, L. J. (2004). Accurate subgrid models for two-phase flow in heterogeneous reservoirs. *Spe Journal*, *9*(02), 219-226. https://doi.org/10.2118/88363-PA

Elmorsy, M., El-Dakhakhni, W., & Zhao, B. (2023). Rapid Permeability Upscaling of Digital Porous Media via Physics-Informed Neural Networks. *Water Resources Research*, *59*(12), e2023WR035064. https://doi.org/10.1029/2023WR035064

Fuks, O., Ibrahima, F., Tomin, P., & Tchelepi, H. A. (2019). Analysis of travel time distributions for uncertainty propagation in channelized porous systems. *Transport in Porous Media*, *126*, 115-137. https://doi.org/10.1007/s11242-018-1052-z

Gel'fand, I. M. (1959). Some problems in the theory of quasi-linear equations. *Uspekhi Matematicheskikh Nauk*, *14*(2), 87-158. https://doi.org/10.1090/trans2/029/12

Gray, W. G., & Miller, C. T. (2014). *Introduction to the thermodynamically constrained averaging theory for porous medium systems* (Vol. 696). Springer. https://doi.org/10.1007/978-3-319-04010-3

Hussain, F., Cinar, Y., & Bedrikovetsky, P. (2012). A semi-analytical model for two phase immiscible flow in porous media honouring capillary pressure. *Transport in Porous Media*, *92*, 187-212. https://doi.org/10.1007/s11242-011-9897-4

Ingsøy, P., Gauchet, R., & Lake, L. W. (1994). Pseudofunctions and Extended Dietz Theory for Gravity-Segregated Displacement in Stratified Reservoirs. *SPE Reservoir Engineering*, *9*(01), 67-72. https://doi.org/10.2118/23601-pa

Jiang, F., Guo, Y., Tsuji, T., Kato, Y., Shimokawara, M., Esteban, L., Seyyedi, M., Pervukhina, M., Lebedev, M., & Kitamura, R. (2023). Upscaling Permeability Using Multiscale X-Ray-CT Images With Digital Rock Modeling and Deep Learning Techniques. *Water Resources Research*, *59*(3), e2022WR033267. https://doi.org/10.1029/2022WR033267

Johns, R. T. (1992). *Analytical theory of multicomponent gas drives with two-phase mass transfer*. Stanford University.

Johnson, E., Bossler, D., & Bossler, V. N. (1959). Calculation of relative permeability from displacement experiments. *Transactions of the AIME*, *216*(01), 370-372. https://doi.org/10.2118/1023-G

Jones, S., & Roszelle, W. (1978). Graphical techniques for determining relative permeability from displacement experiments. *Journal of Petroleum Technology*, *30*(05), 807-817. https://doi.org/10.2118/6045-PA

Kurbanov, A. (1961). On some generalization of the equations of flow of a two-phase liquid in porous media. *Collected Research Papers on Oil Recovery, VNINeft*, *15*, 32-38.

Lake, L. W., Johns, R., Rossen, B., & Pope, G. A. (2014). *Fundamentals of enhanced oil recovery* (Vol. 1). Society of Petroleum Engineers Richardson, TX.

Lax, P. D. (1973). *Hyperbolic systems of conservation laws and the mathematical theory of shock waves*. SIAM.

Li, H., & Durlofsky, L. J. (2016). Upscaling for compositional reservoir simulation. *Spe Journal*, *21*(03), 0873-0887. https://doi.org/10.2118/173212-PA

Logan, J. D. (2008). *An introduction to nonlinear partial differential equations* (Vol. 89). John Wiley & Sons.

Mijic, A., & LaForce, T. C. (2012). Spatially varying fractional flow in radial CO2-brine displacement. *Water Resources Research*, *48*(9). https://doi.org/10.1029/2011WR010961

Mijic, A., LaForce, T. C., & Muggeridge, A. H. (2014). CO2 injectivity in saline aquifers: The impact of non-Darcy flow, phase miscibility, and gas compressibility. *Water Resources Research*, *50*(5), 4163-4185. https://doi.org/10.1002/2013WR014893

Moreno, Z., & Rabinovich, A. (2021). Evaluating numerical simulation errors of CO2-brine flow with capillary heterogeneity using a 1D semi-analytical solution. *International Journal of Greenhouse Gas Control*, *110*, 103416. https://doi.org/10.1016/j.ijggc.2021.103416

Moslehi, M., de Barros, F. P., Ebrahimi, F., & Sahimi, M. (2016). Upscaling of solute transport in disordered porous media by wavelet transformations. *Advances in Water Resources*, *96*, 180-189. https://doi.org/10.1016/j.advwatres.2016.07.013

Oleinik, O. A. e. (1959). Uniqueness and stability of the generalized solution of the Cauchy problem for a quasi-linear equation. *Uspekhi Matematicheskikh Nauk*, *14*(2), 165-170.

Polyanin, A. D., Kutepov, A. M., Kazenin, D., & Vyazmin, A. (2001). *Hydrodynamics, mass and heat transfer in chemical engineering*. CRC Press.

Polyanin, A. D., & Manzhirov, A. V. (2006). *Handbook of mathematics for engineers and scientists*. Chapman and Hall/CRC.

Polyanin, A. D., & Zaitsev, V. F. (2003). *Handbook of nonlinear partial differential equations: exact solutions, methods, and problems*. Chapman and Hall/CRC.

Rabinovich, A., Itthisawatpan, K., & Durlofsky, L. J. (2015). Upscaling of CO2 injection into brine with capillary heterogeneity effects. *Journal of Petroleum Science and Engineering*, *134*, 60-75. https://doi.org/10.1016/j.petrol.2015.07.021

Rabinovich, A., Li, B., & Durlofsky, L. J. (2016). Analytical approximations for effective relative permeability in the capillary limit. *Water Resources Research*, *52*(10), 7645-7667. https://doi.org/10.1002/2016WR019234

Rapoport, L., & Leas, W. (1953). Properties of linear waterfloods. *Journal of Petroleum Technology*, *5*(05), 139-148. https://doi.org/10.2118/213-G

Rasaei, M. R., & Sahimi, M. (2009). Upscaling of the permeability by multiscale wavelet transformations and simulation of multiphase flows in heterogeneous porous media. *Computational Geosciences*, *13*, 187-214. https://doi.org/10.1007/s10596-008-9111-0

Rezapour, A., Ortega, A., & Sahimi, M. (2019). Upscaling of geological models of oil reservoirs with unstructured grids using lifting-based graph wavelet transforms. *Transport in Porous Media*, *127*, 661-684. https://doi.org/10.1007/s11242-018-1219-7

Ringrose, P. (2020). How to store CO2 underground: Insights from early-mover CCS projects. https://doi.org/10.1007/978-3-030-33113-9

Roberts, A. (2015). Macroscale, slowly varying, models emerge from the microscale dynamics. *IMA Journal of Applied Mathematics*, *80*(5), 1492-1518. https://doi.org/10.1093/imamat/hxv004

Roberts, A. (2022). Embed to rigorously and accurately homogenise quasi-periodic multi-scale heterogeneous PDEs, with computer algebra. *arXiv preprint arXiv:2209.02822*. https://doi.org/10.48550/arXiv.2209.02822

Roberts, A. (2024). Construct accurate multi-continuum micromorphic homogenisations in multi-D space-time with computer algebra. *arXiv preprint arXiv:2407.03483*. https://doi.org/10.48550/arXiv.2407.03483

Roberts, A., & Bunder, J. (2017). Slowly varying, macroscale models emerge from microscale dynamics over multiscale domains. *IMA Journal of Applied Mathematics*, *82*(5), 971-1012. https://doi.org/10.1093/imamat/hxx021

Rossen, W., Johns, R., Kibodeaux, K., Lai, H., & Tehrani, N. M. (2008). Fractional-flow theory applied to non-Newtonian IOR processes. ECMOR XI-11th European Conference on the Mathematics of Oil Recovery,

Rossen, W., Venkatraman, A., Johns, R., Kibodeaux, K., Lai, H., & Tehrani, N. M. (2011). Fractional flow theory applicable to non-Newtonian behavior in EOR processes. *Transport in Porous Media*, *89*, 213-236. https://doi.org/10.1007/s11242-011-9765-2

Shapiro, A., & Bedrikovetsky, P. (2008). Elliptic random-walk equation for suspension and tracer transport in porous media. *Physica A: Statistical Mechanics and its Applications*, *387*(24), 5963-5978. https://doi.org/10.1016/j.physa.2008.07.013

Shapiro, A., Bedrikovetsky, P., Santos, A., & Medvedev, O. (2007). A stochastic model for filtration of particulate suspensions with incomplete pore plugging. *Transport in Porous Media*, *67*, 135-164. https://doi.org/10.1007/s11242-006-0029-5

Shapiro, A., & Yuan, H. (2012). Application of stochastic approaches to modelling suspension flow in porous media. In *Statistical mechanics and random walks: Principles, processes and applications* (pp. 1-36). Nova Science Publishers.

Shapiro, A. A. (2022). Continuous upscaling of the 3D diffusion equation in a heterogeneous medium. *Chemical Engineering Science*, *248*, 117247. https://doi.org/10.1016/j.ces.2021.117247

Shapiro, A. A. (2024). On the upscaling of the diffusion equation in a heterogeneous medium by the two different methods. *Physics of Fluids*, *36*(2). https://doi.org/10.1063/5.0174651

Subramanian, S. K., Johns, R. T., & Dindoruk, B. (1999). Solution and upscaling of compositional and immiscible displacements in composite media. *Petroleum Geoscience*, *5*(3), 287-291. https://doi.org/10.1144/petgeo.5.3.287

Thiele, M., & Batycky, R. (2001). Discussion of streamline simulation: A technology update. *Journal of Petroleum Technology*, *53*(05), 26-27. https://doi.org/10.2118/0501-0026-JPT

Thiele, M., Batycky, R., Blunt, M., & Orr Jr, F. (1996). Simulating flow in heterogeneous systems using streamtubes and streamlines. *SPE Reservoir Engineering*, *11*(01), 5-12. https://doi.org/10.2118/27834-PA

Tran-Duc, T., Bunder, J., & Roberts, A. J. (2024). Efficient computational homogenisation of 2D beams of heterogeneous elasticity using the patch scheme. *International Journal of Solids and Structures*, *292*, 112719. https://doi.org/10.1016/j.ijsolstr.2024.112719

Wachmann, C. (1964). A mathematical theory for the displacement of oil and water by alcohol. *Society of Petroleum Engineers Journal*, *4*(03), 250-266.

Wei, Y., & Rabinovich, A. (2023). The inverse problem of permeability identification for multiphase flow in porous media. *Physics of Fluids*, *35*(7). https://doi.org/10.1063/5.0153939

Welge, H. J. (1952). A simplified method for computing oil recovery by gas or water drive. *Journal of Petroleum Technology*, *4*(04), 91-98. https://doi.org/10.2118/124-G

Yang, H. J., Tchelepi, H. A., & Tartakovsky, D. M. (2022). Method of Distributions for Two-Phase Flow in Heterogeneous Porous Media. *Water Resources Research*, *58*(12), e2022WR032607. https://doi.org/10.1029/2022WR032607

Yortsos, Y. C. (1995). A theoretical analysis of vertical flow equilibrium. *Transport in Porous Media*, *18*(2), 107-129. https://doi.org/10.1007/BF01064674

Zhang, X., Shapiro, A., & Stenby, E. H. (2011). Upscaling of two-phase immiscible flows in communicating stratified reservoirs. *Transport in Porous Media*, *87*, 739-764. https://doi.org/10.1007/s11242-011-9713-1